The Linear and Self-Consistent Nonlinear Theory of the Electron Cyclotron Maser Instability

P. SPRANGLE AND A. T. DROBOT

Abstract—**In this paper the linear and nonlinear theory of the electron cyclotron maser instability is considered. The configuration used to study the maser instability consists of relativistic electrons gyrating about and drifting along a uniform magnetic field within a parallel plate waveguide. Relativistic effects associated with the gyrating electrons are responsible for excitation of the transverse electric mode in the waveguide. Linear theory shows that the growth rate maximizes when the axial beam velocity coincides with the axial wave group velocity of the excited electromagnetic wave. This allows us to perform the nonlinear analysis in a frame where both the axial wave number and axial beam velocity vanish. We have found that the maser instability exists only if the perpendicular beam energy exceeds a threshold value. Our analysis also describes the temporal nonlinear evolution of the field amplitude and frequency of a single excited wave. The nonlinear wave dynamics are self-consistently determined from the nonlinear particle orbits through the force and wave equations. The nonlinear analysis shows that there are two possible mechanisms for the saturation of the unstable wave: 1) depletion of the available free energy associated with the rotating particles and 2) phase trapping of the gyrating electrons in the wave. The initial beam parameters determine which of the two mechanisms is responsible for saturation. Competition between the two saturation mechanisms leads to a peaking in the energy conversion efficiency as a function of beam energy. Numerical results of the nonlinear formalism show that energy conversion efficiencies from the particles to the wave can be as high as 60 percent in the beam frame. Furthermore, by appropriately contouring the external magnetic field, among other things, efficiencies as high as 70 percent can be realized.**

I. INTRODUCTION

IN THE cyclotron maser instability electromagnetic radiation is generated by relativistic electrons gyrating about an external magnetic field. The bunching process in the maser instability is a relativistic effect due to the energy-dependent electron cyclotron frequency. The excited wave frequency is near the Doppler-shifted electron cyclotron frequency of the gyrating electrons. The free energy for the maser instability resides in the rotational energy of the electrons. To make this source of energy from a streaming electron beam available for the generation of radiation, a redistribution of electron energy is needed. For example, converting streaming to rotational energy can be accomplished by propagating the electron beam through a spatially varying external magnetic field. This conversion process is the classical equivalent of producing inverted population levels in molecular masers by pumping.

The electron cyclotron maser instability is particularly promising for efficient generation of millimeter and submillimeter radiation. In this part of the electromagnetic spectrum more conventional devices are severely limited in both power and efficiency. Such devices as the traveling wave tube or magnetron rely on a slow wave structure for their operation. The radiation wavelength from these devices is typically on the order of the structure period. Power density as well as voltage breakdown considerations place a lower limit on the dimensions of the structure depending on the efficiency and radiated power requirements. Therefore, these slow wave devices are not particularly suited for efficient generation of large fluxes of radiation at millimeter and submillimeter wavelengths. The electron cyclotron maser mechanism, on the other hand, does not rely on the fine structure of a waveguide or cavity, and thus efficient operation at millimeter and submillimeter wavelengths is possible.

The linear mechanism of the cyclotron maser was first proposed by Twiss [1] classically and later quantum mechanically by Schneider [2]. Shortly after the work of Twiss, Gaponov published a paper on the classical theory of the cyclotron maser [3]. In 1959, Pantell published what was perhaps the first experimental work involving the electron cyclotron maser mechanism [4]. In this experiment radiation at 2.5–4.0 GHz was produced from a 1-kV 3-μP electron beam. Pantell suggested that the radiation was caused by the coupling of the TE_{11} waveguide mode to the backward traveling cyclotron wave on the magnetized beam. It was Hirshfield and Wachtel who performed the first experiment that definitely confirmed the existence of the electron cyclotron maser mechanism [5]. Apparently, because of a lack of understanding of the nonlinear dynamics, the observed efficiencies in the initial experiments were low, $\lesssim 2$ percent. In this early work the cyclotron maser was operated both as an oscillator and as an amplifier at millimeter wavelengths [5]–[9]. The radiated power achieved in these experiments was as high as 1 kW [8]. Nonpulsed low-current electron beams were used throughout the early experiments.

The advent of intense pulsed relativistic electron beams has renewed interest in the cyclotron maser instability as a source of high-power microwave radiation. These intense electron beams use a field emission diode and typically carry a current of $\lesssim 100$ kA, a voltage of $\lesssim 5$ MeV, and last for approximately 50 ns. Microwave radiation at multimegawatt levels [10] and as high as 1 GW [11] has been produced using these intense relativistic electron beams. By operating the cyclotron maser as a single-stage amplifier, a 17-dB gain was obtained [12]. In general, the emitted radiation was narrow band with a coherence time >50 ns,

Manuscript received January 20, 1977. This work was supported by the Office of Navy Material Command Task RF34372401 and by the Army Ballistic Missile Defense Advance Technology Center Project No. 8X363304D215.

P. Sprangle is with the Plasma Dynamics Branch, Plasma Physics Division, Naval Research Laboratory, Washington, DC 20375.

A. T. Drobot is with Science Applications, Inc., McLean VA 22101.

and was also spatially coherent [13]. None of the experiments using pulsed intense electron beams attained efficiencies greater than about 2 percent. Our analysis shows that there are a number of reasons for the observed low efficiencies with intense relativistic electron beams.

The highest reported efficiencies with a cyclotron maser device were obtained in the Soviet Union using thermionic diodes [14], [15]. In the experiments by Zaytsev *et al.* [14], 12-kW CW at 2.78 mm was reported using the fundamental cyclotron mode. Experimental efficiencies in this case were 31 percent. Interaction at the second cyclotron harmonic produced an output power of 1.5 kW CW at 0.92 mm with an efficiency of 6.2 percent. Using the second cyclotron harmonic, Kisel' *et al.* [15] obtained output powers of 10 kW CW at 8.9 mm with efficiencies of 40 percent. In the pulsed electron mode, power levels of 30 kW at 43 percent efficiency were reported.

Work on the linear theory of the cyclotron maser shows that the instability is due to the coupling of the supraluminous TE waveguide mode and a beam cyclotron mode [10], [16]–[19]. The instability may be either absolute or convective in nature. For a review of the theory on excited nonlinear oscillators as applied to the cyclotron maser, see the article by Gaponov *et al.* [20].

To our knowledge, the first nonlinear evaluation of the electron cyclotron maser mechanism involved numerical integration of the electron orbits in fields of either constant amplitude and/or constant frequency [16], [21]–[25]. These nonlinear theories do not fully treat the particles and wave dynamics in an inherently self-consistent manner.

In this paper a comprehensive study of the self-consistent nonlinear evolution of the electron cyclotron maser instability is presented. We have included both a time-dependent frequency shift and a time-dependent field amplitude in our analysis. A rather simple physical picture of the nonlinear behavior of this instability shows that there are two mechanisms responsible for wave saturation. The analysis is self-consistent in that the particle and wave dynamics are treated as a unit. Our parameter study indicates that the maser instability can be an efficient mechanism for the production of high-power radiation, particularly at millimeter and submillimeter wavelengths. Saturation efficiencies at the fundamental waveguide mode and cyclotron mode are obtained. A method of externally controlling the saturation process, and thereby further improving conversion efficiencies, is discussed.

The physical mechanism of the electron cyclotron maser is described in Section II. Properties of the linear dispersion relation are discussed in Section III. Here simple expressions for the linear growth rate and frequency shift are obtained. The linear theory indicates that the growth rate maximizes when the axial beam velocity is equal to the group velocity of the excited wave. This fact can be used to simplify the analysis by performing all calculations in the beam frame which now coincides with the cutoff frame where the axial wave number k_0 vanishes. The results are then transformed back to the laboratory frame. In Section IV we derive the equations for the nonlinear growth rate and frequency shift of the excited wave. The nonlinear single wave formalism treats both the particle and wave dynamics self-consistently. The equivalence of our temporal model with the steady-state spatial growth of a wave in an amplifier is pointed out. A number of simplifying assumptions, such as the single wave approximation and neglect of initial beam temperature and space charge effects, have been made in our analysis. The conditions for the validity of these approximations are discussed in Section V. Section VI describes the two nonlinear saturation processes of the cyclotron maser instability. There we show that the depletion of free energy and/or particle phase trapping is responsible for wave saturation. The dominant mechanism depends on the initial choice of beam parameters. Simple analytic expressions for the field amplitude at saturation are obtained. From the slow time scale orbit equations we obtain a constant of the motion for a fixed amplitude and frequency field. This constant is used to examine the nonlinear particle orbits in phase space. Section VII contains the numerical results of our formalism for a wide range of beam parameters. These results include field amplitudes and efficiencies at saturation. Comparison of these results with the analytic expressions given in Section VI is made. Methods for improving the efficiency at saturation are also discussed and examples given. Section VIII contains a brief discussion of our results as well as possible applications for the cyclotron maser. The low experimental efficiencies with intense relativistic electron beams for the cyclotron maser are discussed in the light of our theoretical results. A detailed example showing how our results can be applied to practical situations to estimate power efficiencies and levels of the radiation field is given. In Appendix A we show that the linear dispersion relation can be recovered from the nonlinear formalism. Because our analysis is performed in the beam cutoff frame, we include a derivation of the efficiency transformation from the beam frame to the laboratory frame in Appendix B.

II. Physical Mechanism

Insight into the physical mechanism responsible for the electron cyclotron maser instability can be obtained from the particle trajectories shown in Fig. 1(a) and (b). This figure shows the orbit dynamics of sample electrons initially uniformly distributed along a gyro orbit. The electrons are rotating in the counter clockwise direction about a uniform and constant magnetic field $B_0\hat{e}_z$. Without loss of generality, we assume the electron velocity in the z direction to be zero. The initial radius of the sample electron ring is the Larmor radius $r_{0L} = v_{0\perp}/(\Omega_0/\gamma_{0\perp})$ where $v_{0\perp}$ is the initial perpendicular velocity, $\Omega_0 = |e|B_0/m_0c$ is the nonrelativistic cyclotron frequency, and $\gamma_{0\perp} = (1 - v_{0\perp}^2/c^2)^{-1/2}$ is the relativistic factor.

The introduction of a small constant amplitude electric field $E_y(t) = \varepsilon_0 \cos(\omega_0 t)\hat{e}_y$, as shown in Fig. 1(a), will alter the particle orbits. We first examine the particle trajectories when the frequency of the electric field is equal to the initial relativistic cyclotron frequency $\omega_0 = \Omega_0/\gamma_{0\perp}$.

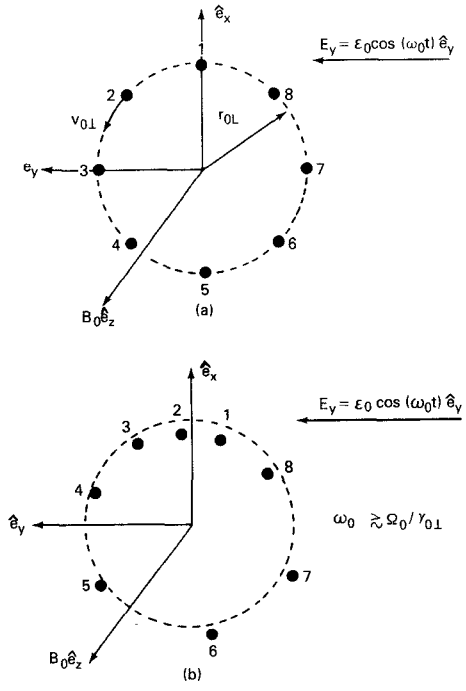

Fig. 1. The mechanism responsible for the electron cyclotron maser illustrated by orbits of test particles in velocity space in the presence of a small external field. (a) Initial particle positions. (b) Bunched particles after several cycles.

The time rate of change of the particle energy is $d\varepsilon_p/dt = -|e|v_y(t)E_y(t)$ where $v_y(t)$ is the y component of particle velocity. With the initial choice of field direction shown in Fig. 1(a), particles 8, 1, and 2 will lose energy and tend to spiral inward. The relativistic cyclotron frequency of these particles will increase, since $\gamma_\perp$ decreases, and their phase will tend to slip ahead of the wave. Particles 4, 5, and 6, on the other hand, will gain energy, their cyclotron frequency will decrease, and they will tend to spiral outward. The phase of these particles will tend to slip behind the wave. After an integral number of wave periods, the particles will become bunched around the positive y axis. Particle bunching is, therefore, caused by relativistic effects, since the rotational frequency of the electrons is energy dependent.

To obtain a net exchange of energy between the particles and wave, ω_0 must be slightly greater than $\Omega_0/\gamma_{0\perp}$. If $\omega_0 \gtrsim \Omega_0/\gamma_{0\perp}$, the particles on the average traverse a coordinate space angle less than 2π in a wave period $2\pi/\omega_0$. All the particles will then slip behind the wave, and the distribution of particles after an integral number of wave periods will be bunched in the upper half plane as shown in Fig. 1(b). As a result of the phase slippage between the particles and the field, the net kinetic energy of the ensemble of particles decreases. Conservation of total energy implies that the field amplitude increases, resulting in instability. If ω_0 remains greater than $\Omega_0/\gamma_\perp$, the particles will continue to slip behind the wave.

Depending on the initial beam parameters, the group of bunched beam particles may 1) continue to slip behind the wave, or 2) initially slip behind the wave, reverse itself, and begin to oscillate about the positive y axis. In either case, the bunched particles will eventually appear in the lower half of the transverse plane after an integral number of wave periods. When this occurs, the particles will gain energy and the wave amplitude will begin to decrease.

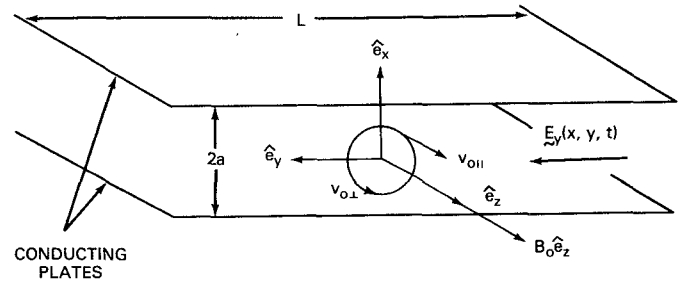

Fig. 2. The electron cyclotron maser configuration in plane geometry.

III. Linear Theory

Using the Maxwell–Vlasov equations, the linear theory of the electron cyclotron maser instability has been derived in both cylindrical [10] and Cartesian geometry [19]. The electron beam and waveguide configuration employed in [19] and shown in Fig. 2 is basically the same model used in the present nonlinear analysis. In Fig. 2 a beam of gyrating and drifting particles is assumed to have the same perpendicular velocity $v_{0\perp}$ and parallel velocity $v_{0\parallel}$ with respect to the applied axial magnetic field B_0. The guiding centers of the particles lie midway between the two conducting plates. The system of particles and fields is assumed independent of the spatial y variable. The field components within the waveguide are those of a TE_{0n} mode (i.e., E_y, B_z, and B_x are the only nonvanishing field components). The functional dependence of the fields on z and t has the form $\exp(i(k_0 z - \omega t))$. The linear dispersion relation in the laboratory frame for the above configuration is

$$\omega^2 - c^2(k_0^2 + k_n^2) = \delta_{nl}(\omega_b^2/\gamma_0) \cdot \left[\frac{(\omega - k_0 v_{0\parallel})Q_{nl}}{(\omega - k_0 v_{0\parallel} - l\Omega_0/\gamma_0)} - \frac{\beta_{0\perp}^2(\omega^2 - c^2k_0^2)W_{nl}}{(\omega - k_0 v_{0\parallel} - l\Omega_0/\gamma_0)^2}\right] \quad (1)$$

where $k_n = \pi n/2a$ is the perpendicular wave number, $n = 1,2,3,\cdots$ is the waveguide mode number, $\delta_{ln} = (1 + (-1)^{n+l})$, $\omega_b^2 = 4\pi|e|\sigma_0/m_0 a$ is the modified plasma frequency, σ_0 is the surface charge density of the beam in the x–y plane, $l = 1,2,3$ is the magnetic harmonic number, $\gamma_0 = (1 - v_{0\parallel}^2/c^2 - v_{0\perp}^2/c^2)^{-1/2}$, $\Omega_0 = |e|B_0/m_0 c$, $\beta_{0\perp} = v_{0\perp}/c$, $Q_{nl} = x_n(l^2/x_n^2 - 1)\,d(J_l(x_n))^2/dx$, $W_{nl} = (dJ_l(x_n)/dx_n)^2$, $x_n = \beta_{0\perp} c k_n/(\Omega_0/\gamma_0)$, and J_l is the Bessel function of order l. If $n + l$ is odd, the TE_{0n} mode is stable since the right-hand side of (1) vanishes [26]. The first term in the bracket on the right-hand side of (1) is always stabilizing while the second term is always destabilizing. Furthermore, the frequency of the unstable wave in the rest frame of the electrons is slightly greater than the cyclotron frequency, $\gamma_0(\omega - k_0 v_{0\parallel}) \gtrsim \Omega_0$. We have seen in Section II that this requirement is necessary for a phase slippage to occur between the particles and field. It is clear from the dispersion relationship in (1) that the maximum growth rate of the modified TE_{0n} mode occurs for frequencies and wave numbers near the intersection of the vacuum waveguide

mode $\omega^2 - c^2(k_0^2 + k_n^2) = 0$, and the cyclotron mode $\omega - k_0 v_{0\parallel} - l\Omega_0/\gamma_0 = 0$. When the perpendicular velocity of the particles $v_{0\perp}$ vanishes, the cyclotron wave is a positive energy wave. Since the waveguide mode is also a positive energy wave, there can be no instability for $v_{0\perp} = 0$. If, however, $v_{0\perp} \neq 0$, the cyclotron mode splits into a positive and negative energy polarity wave as can be seen from the fact that $(\omega - k_0 v_{0\parallel} - l\Omega_0/\gamma_0)^2$ appears in the denominator of the destabilizing term of (1). The coupling of the negative energy cyclotron wave and positive energy waveguide mode is responsible for the instability. In the limit of vanishing beam density $\omega_b \to 0$, or vanishing perpendicular velocity $v_{0\perp} \to 0$, the opposite energy polarity cyclotron waves coalesce and become degenerate.

Seeking a solution to (1) near the intersection of the modes, we set $\omega = \omega_0 + \delta\omega_0$ where $|\delta\omega_0| \ll \omega_0$ and $\omega_0 = c(k_0^2 + k_n^2)^{1/2} = k_0 v_{0\parallel} + l\Omega_0/\gamma_0$. Substituting $\omega = \omega_0 + \delta\omega_0$ into (1) and keeping terms to order $(\delta\omega_0)^3$ yields the following relation:

$$\delta^3\omega_0 - 3\Delta^2\omega_0\delta\omega_0 + 3Z_{nl}\Delta^2\omega_0 = 0 \qquad (2)$$

where

$$\Delta\omega_0 = (l\Omega_0/\gamma_0(\delta_{nl}\omega_b^2/(6\gamma_0\omega_0))Q_{nl})^{1/2}$$

and

$$Z_{nl} = (x_n/l)^2(W_{nl}/Q_{nl})(l\Omega_0/\gamma_0).$$

The solutions of (2) yield complex roots when $Z_{nl} > (2/3)\Delta\omega_0$. This condition can be stated as a threshold condition for instability, requiring that the perpendicular velocity be greater than a critical value [27],

$$\beta_{0\perp} > \beta_{\perp,\mathrm{crit}}$$

where

$$\beta_{\perp,\mathrm{crit}} = l(\Omega_0/\gamma_0)(Q_{nl}/W_{nl})^{1/2} \cdot [(2/27)\delta_{nl}\omega_b^2 Q_{nl}/(\gamma_0\omega_0 l\Omega_0/\gamma_0)]^{1/4}/ck_n.$$

At the critical value of $\beta_\perp$ the stabilizing and destabilizing terms in (1) just balance each other. The beam has no free energy available for driving the instability when $\gamma_{0\perp} = \gamma_{\perp,\mathrm{crit}}$, where $\gamma_{\perp,\mathrm{crit}} = (1 - \beta_{\perp,\mathrm{crit}}^2)^{-1/2}$. The roots of (2) can be easily evaluated in two regimes: 1) $\beta_{0\perp} \gtrsim \beta_{\perp,\mathrm{crit}}$, and 2) $\beta_{0\perp} \gg \beta_{\perp,\mathrm{crit}}$. In the first regime, the perpendicular energy of the beam is close to the critical value and the saturation is caused by the depletion of free energy. In the second regime, the perpendicular energy of the beam is well above the critical value and, as we will show in Section VI, the saturation mechanism for the instability is phase trapping of the particles by the excited wave.

Case 1)

Here, $\beta_{0\perp} \gtrsim \beta_{\perp,\mathrm{crit}}$ and the second term on the right-hand side of (1) is larger but comparable to the first term. The linear frequency shift and growth rate take the form

$$\Delta\omega_i = \mathrm{Re}\,(\delta\omega_0)_i = ((3/2)Z_{nl}\Delta^2\omega_0)^{1/3} \approx \Delta\omega_0 \qquad (3a)$$

$$\Gamma_i = \mathrm{Im}\,(\delta\omega_0)_i = 3^{-1/2}(\Delta\omega_0)^{2/3}(3Z_{nl}/2)^{-2/3}((3Z_{nl}/2)^2 - \Delta^2\omega_0)^{1/2} \approx (Z_{nl}\Delta\omega_0 - 2\Delta^2\omega_0/3)^{1/2}. \qquad (3b)$$

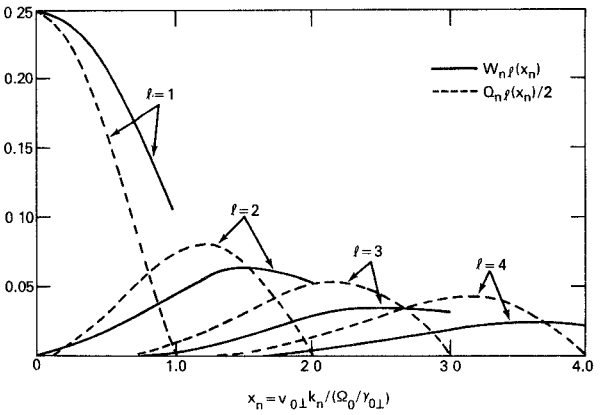

Fig. 3. The functions $Q_{nl}(x_n)$ and $W_{nl}(x_n)$ versus x_n for $l = 1, 2, 3, 4$.

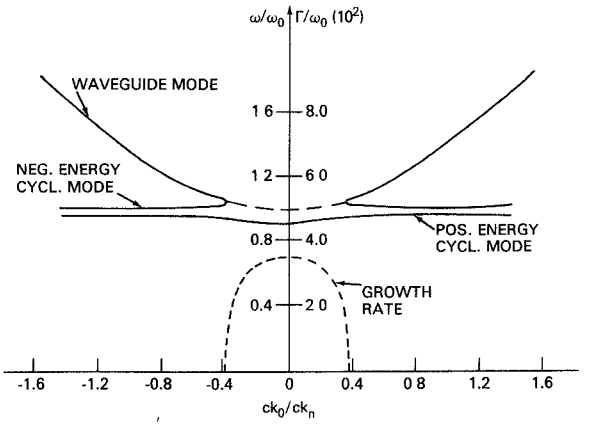

Fig. 4. Typical dispersion curve for cyclotron maser instability. This case is for $\gamma_{0\perp} = 1.2$, $\omega_b/\sqrt{\gamma_{0\perp}} = 0.05\omega_0$, $\omega_0 = ck_n = l\Omega/\gamma_{0\perp}$, and $l = n = 1$.

The growth rate for this case is proportional to the fourth root of the surface charge density.

Case 2)

Here, $\beta_{0\perp} \gg \beta_{\perp,\mathrm{crit}}$ and the second term on the right-hand side of (2) dominates. The linear frequency shift and growth rate of the wave are

$$\Delta\omega_{ii} = \mathrm{Re}\,(\delta\omega_0)_{ii} = (1/2)(3Z_{nl}\Delta^2\omega_0)^{1/3} \qquad (4a)$$

$$\Gamma_{ii} = \mathrm{Im}\,(\delta\omega_0)_{ii} = 3^{1/2}/2(3Z_{nl}\Delta^2\omega_0)^{1/3}. \qquad (4b)$$

The growth rate for this case is proportional to the third root of the surface charge density σ_0.

The condition that the nth waveguide mode and the lth synchronous mode intersect on the dispersion curve limits the value of x_n. It is easy to show that x_n is bounded by $0 \leq x_n \leq l$. Fig. 3 depicts the functions W_{nl} and Q_{nl} as functions of x_n for $l = 1$, 2, 3, and 4. Fig. 4 shows the dispersion diagram for the cyclotron maser instability when $v_{0\parallel} = 0$, $\omega_0 = ck_n = l\Omega_0/\gamma_0$ and $l = n = 1$. Note that the cyclotron mode splits into two branches of negative and positive energy polarity. The negative energy cyclotron mode couples to the positive energy TE guide mode resulting in an instability. The growth rate maximizes at $k_0 = 0$. If the cyclotron frequency were greater than the guide cutoff frequency $\Omega_0/\gamma_{0\perp} > ck_n$, the growth rate

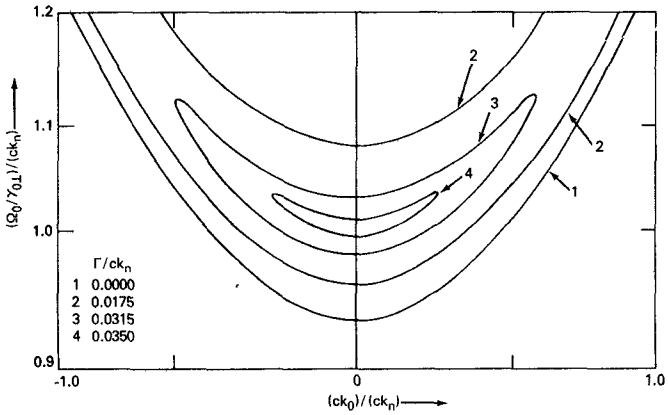

Fig. 5. Contours of the growth rate for the cyclotron maser instability versus the parallel wave number and the cyclotron frequency. This case is for $\gamma_{0\perp} = 1.2$ and $\omega_b/\sqrt{\gamma_{0\perp}} = 0.05\omega_0$, where $\omega_0 = ck_n$ and $l = n = 1$.

would have two peaks at $|k_0| > 0$, symmetric about the $k_0 = 0$ axis. The maximum growth rate for $\Omega_0/\gamma_{0\perp} > ck_n$ is always less than the maximum growth rate for $\Omega_0/\gamma_{0\perp} = ck_n$. This can be seen in Fig. 5, where growth rate contours are shown as functions of $(\Omega_0/\gamma_{0\perp})/(ck_n)$ and (ck_0/ck_n). We note that, in general, the growth rate is maximum when the wave group velocity v_g equals the axial beam velocity $v_{0\parallel}$. This becomes apparent if we transform to the beam frame ($v_{0\parallel} = 0$) and note that for fixed $\beta_{0\perp}$ and k_n, the growth rate is largest when $k_0 = 0$ (i.e., when $\omega_0 = l\Omega_0/\gamma_0 = ck_n$). At $k_0 = 0$, the group velocity vanishes and, therefore, $v_g = v_{0\parallel} = 0$ in this frame. Since both v_g and $v_{0\parallel}$ transform in the same way, the growth rate maximizes when $v_g = v_{0\parallel}$ in all frames.

IV. Nonlinear Formalism

In this section the basic equations governing the nonlinear behavior of the electron cyclotron maser instability are derived using a single wave model. The validity of the single wave approach will be examined in Section V.

In our procedure, we express the nonlinear dynamics of a single wave in terms of an ensemble average of the nonlinear particle orbits. The particle orbits are related to the fields through the relativistic Lorentz force equations. The resulting wave and force equations are then numerically solved to obtain the self-consistent behavior of the particles and the field. This analysis describes the nonlinear evolution of the field amplitude and frequency as a function of time. The beam and waveguide configuration shown in Fig. 2 is chosen as our basic model.

We have noted in Section III that the linear growth rate for the excited TE_{0n} mode maximizes when the axial beam velocity and the wave group velocity are equal. We chose to analyze this situation since we are interested in the regime of maximum wave growth. Furthermore, for convenience, we transform to a frame in which both the axial beam velocity and wave group velocity vanish. Since the group velocity is now zero in this frame (cutoff frame), we note that the axial wave number of the wave is also zero. The electric field, in the cutoff frame, of the vacuum waveguide mode has the form

$$E_y(x,t) = -E_0(t)\cos(\omega_0 t + \alpha(t))\sin(k_n(x-a)) \quad (5a)$$

where $k_n = \pi n/(2a)$ and n is a positive integer such that $E_y(x,t)$ satisfies the appropriate boundary conditions at $x = \pm a$. In (5a) the frequency ω_0 is a constant, while the amplitude $E_0(t)$ and the frequency shift $\partial\alpha(t)/\partial t$ are weak functions of time (e.g., $\partial \ln (E_0(t))/\partial t$, $\partial\alpha(t)/\partial t \ll \omega_0$). The amplitude $E_0(t)$ can be expressed as

$$E_0(t) = \varepsilon_0 \exp \int_0^t \Gamma(t')\,dt' \quad (5b)$$

where ε_0 is the initial field amplitude and $\Gamma(t)$ is the time-dependent growth rate. We note that in the linear regime of the instability the frequency shift and growth rate are constant and equal to their linear values $\partial\alpha(t)/\partial t = \Delta\omega_L$ and $\Gamma(t) = \Gamma_L$.

Associated with the electric field in (5a) is the vector potential $A_y(x,t)$ given by

$$A_y(x,t) = (c/\omega_0)\{(1 - \dot{\alpha}/(\omega_0)E_0\sin(\omega_0 t + \alpha) + (\dot{E}_0/\omega_0)\cos(\omega_0 t + \alpha)\}\sin(k_n(x-a)) \quad (6)$$

where $A_y(x,t)$ is valid to first order in the small parameters $\Gamma(t)/\omega_0$ and $\dot{\alpha}(t)/\omega_0$. The time evolution of $E_0(t)$ and $\alpha(t)$ is determined by the particle current density $J_y(x,t)$ through the wave equation for $A_y(x,t)$:

$$(\partial^2/\partial x^2 - c^{-2}\,\partial^2/\partial t^2)A_y = -4\pi c^{-1}J_y. \quad (7)$$

Substituting (6) into the wave equation and keeping only lowest order terms in the small parameters Γ/ω_0 and $\dot{\alpha}/\omega_0$ yields the relation

$$\{(\omega_0^2 - c^2k_n^2 + (c^2k_n^2 + \omega_0^2)(\dot{\alpha}/\omega_0))E_0\sin(\omega_0 t + \alpha) - (c^2k_n^2 + \omega_0^2)(\dot{E}_0/\omega_0)\cos(\omega_0 t + \alpha)\}\sin(k_n(x-a)) = -4\pi\omega_0 J_y(x,t). \quad (8)$$

The current density for a discrete set of particles is given by

$$J_y(x,t) = -\frac{|e|\sigma_0}{N}\sum_{i=1}^{N} v_y(\phi_i,t)\delta(x - x(\phi_i,t)) \quad (9)$$

where σ_0 is the surface number density in the y–z plane, N is the number of particles on a gyro radius, ϕ_i is the initial velocity space angle of the ith particle measured with respect to the x axis, and $x(\phi_i,t)$ is the x position of the ith particle. In the limit as $N \to \infty$,

$$N^{-1}\sum \to (2\pi)^{-1}\int_0^{2\pi} d\phi_0$$

where ϕ_0 replaces ϕ_i. In (9) the velocity component v_y of the ith particle is a function of only (ϕ_i,t) since we assume an initially cold particle distribution in velocity. Our theory can include an initially thermal particle distribution, which would add an average over the initial velocities in (9). We will show later in (25) that for an initial energy spread $\delta\gamma_\perp \ll 2\gamma_{0\perp}\,\Delta\omega/(\Omega_0/\gamma_{0\perp})$, the particle distribution can be considered monoenergetic at $t = 0$. The present analysis is

valid when the inequality in (25) is satisfied. This does not, however, prevent the particles from thermalizing as the instability develops. The wave equation can be separated into equations for $E_0(t)$ and $\alpha(t)$. By multiplying (8) by $\sin(k_n(x-a))$, integrating across the waveguide from $x=-a$ to $x=a$ and operating on the resulting equation with

$$\int_t^{t+2\pi/(\omega_0+\dot{\alpha})} dt' \begin{Bmatrix} \sin(\omega_0 t' + \alpha(t')) \\ \cos(\omega_0 t' + \alpha(t')) \end{Bmatrix}$$

we arrive at the following expressions, which are valid to order Γ/ω_0, $\dot{\alpha}/\omega_0$:

$$\dot{\alpha}(t) = \frac{\omega_0}{(\omega_0^2 + c^2k_n^2)} \Bigg[c^2k_n^2 - \omega_0^2 + \left\{ \frac{2|e|\sigma_0}{a}\omega_0(\omega_0+\dot{\alpha}) \cdot \int_t^{t+2\pi/(\omega_0+\dot{\alpha})} dt' \langle v_y(\phi_0,t') \cdot \sin(k_n(x(\phi_0,t')-a)) \sin(\omega_0 t' + \alpha(t')) \rangle \right\} \cdot \left\{ \int_t^{t+2\pi/(\omega_0+\dot{\alpha})} E(t') \sin^2(\omega_0 t' + \alpha(t'))\, dt' \right\}^{-1} \Bigg] \tag{10a}$$

$$\Gamma(t) = \frac{\omega_0}{\omega_0^2 + c^2k_n^2} \left\{ \frac{2|e|\sigma_0}{a}\omega_0(\omega_0+\dot{\alpha}) \cdot \int_t^{t+2\pi/(\omega_0+\dot{\alpha})} dt' \cdot \langle v_y(\phi_0,t') \sin(k_n(x(\phi_0,t')-a)) \cos(\omega_0 t' + \alpha(t')) \rangle \right\} \cdot \left\{ \int_t^{t+2\pi/(\omega_0+\dot{\alpha})} E(t') \cos^2(\omega_0 t' + \alpha(t'))\, dt' \right\}^{-1}. \tag{10b}$$

In the preceding equations, $\langle\ \rangle = (2\pi)^{-1}\int_0^{2\pi} d\phi_0$ is the ensemble average over the initial particle phase. We note that the temporal averages in (10a) and (10b) are performed over the actual wave period $2\pi/(\omega_0+\dot{\alpha})$. Equations (10a) and (10b) describe the linear as well as nonlinear evolution of the wave frequency and amplitude in terms of the particle orbits. The only restriction placed on $\Gamma(t)$ and $\alpha(t)$ is that they vary little in a wave period $2\pi/(\omega_0+\dot{\alpha})$.

The right-hand side of (10a) and (10b) contain the details of the particle dynamics which are related to the fields through the relativistic orbit equations. Defining $\beta = \beta_x + i\beta_y$ where $\beta_x = v_x/c$ and $\beta_y = v_y/c$, the relativistic orbit equation can be put into the form

$$d\beta/dt = \frac{i\Omega_0}{\gamma_\perp}\beta + \frac{i|e|B_z(x,t)}{\gamma_\perp m_0 c}\beta \frac{-i|e|}{\gamma_\perp m_0 c} \cdot (1 - \beta(\beta - \beta^*)/2)E_y(x,t) \tag{11}$$

where $\gamma_\perp = (1-\beta\beta^*)^{-1/2}$, $E_y(x,t) = -c^{-1}\,\partial A_y/\partial t$, $B_z(x,t) = \partial A_y/\partial x$, and x is given by $dx/dt = c(\beta+\beta^*)/2$.

We now choose the solution for (11) to be of the form

$$\beta(\phi_0,t) = \beta_\perp(\phi_0,t)\exp(i\phi(\phi_0,t)) \tag{12}$$

where $\beta_\perp(\phi_0,t) = (\beta_x^2 + \beta_y^2)^{1/2} = (\beta\beta^*)^{1/2}$ and

$$\phi(\phi_0,t) = \int_0^t \psi(\phi_0,t')\,dt' + \phi_0 = \tan^{-1}(\beta_y/\beta_x)$$

is the velocity space angle at time t. Substituting (12) into (11) and equating real and imaginary parts, we obtain the following fully relativistic equations for the velocity magnitude and velocity space angle

$$\frac{d\beta_\perp}{dt} = \frac{-|e|E_y(x,t)}{\gamma_\perp^3 m_0 c}\sin\phi(\phi_0,t) \tag{13a}$$

$$\frac{d\phi}{dt} = \frac{\Omega_0}{\gamma_\perp} - \frac{|e|E_y(x,t)}{\gamma_\perp m_0 c\beta_\perp}\cos\phi(\phi_0,t) + \frac{|e|B_z(x,t)}{\gamma_\perp m_0 c} \tag{13b}$$

where $\gamma_\perp = (1-\beta_\perp^2)^{-1/2}$ and $dx/dt = c\beta_\perp\cos\phi(\phi_0,t)$. Equations (5), (10), and (13) form a set of coupled nonlinear equations which describe the evolution of the electron cyclotron maser instability in the single wave model.

In Appendix A we show that the results from linear theory can be recovered from these equations. The orbit equation in (13) when written on the slow time scale yields a constant of the motion which is discussed in Section VI. The constant is useful in forming a qualitative picture of the trapping and saturation process.

The amplitude of the electric $E_0(t)$ can be related to average decrease in particle energy through the energy conservation equation. Conservation of total energy within the waveguide implies that

$$\frac{1}{2a}\int_{-a}^{a}(\varepsilon_f(x,t) + \varepsilon_p(x,t))\,dx = \varepsilon_t \tag{14}$$

where $\varepsilon_f(x,t) = (E_y^2(x,t) + B_z^2(x,t))/8\pi$ is the field energy density, $\varepsilon_p(x,t) = \sigma_0\langle(\gamma(\phi_0,t)-1)\,\delta(x - x(\phi_0,t))\rangle m_0c^2$ is the particle energy density, and $\varepsilon_t = (\sigma_0/2a)(\gamma_0 - 1)m_0c^2$ is the average total energy density. Substituting $E_y = -c^{-1}\,\partial A_y/\partial t$ and $B_z = \partial A_y/\partial x$ into (14), where A_y is given by (6), and performing the spatial average as well as a temporal average, leads to the following expression for $E_0(t)$:

$$E_0(t) = \frac{2m_0c}{|e|}\omega_b\left(1 + \left(\frac{ck_n}{\omega_0}\right)^2(1 - 2\dot{\alpha}/\omega_0)\right)^{-1/2} \cdot (\gamma_{0\perp} - \langle\gamma_\perp(\phi_0,t)\rangle)^{1/2} \tag{15}$$

where $\omega_b = 4\pi|e|^2\sigma_0/(m_0a)$ is a modified plasma frequency and $\gamma_{0\perp}$ is the initial gamma of the particles. In deriving (15), terms of order higher than Γ/ω_0 and $\dot{\alpha}/\omega_0$ have been neglected. Since $ck_n/\omega_0 \approx 1$ and $\dot{\alpha}/\omega_0 \ll 1$, the expression for $E_0(t)$ can be simplified to

$$E_0(t) \approx \frac{\sqrt{8}m_0c}{|e|}\omega_b(\gamma_{0\perp} - \langle\gamma_\perp(\phi_0,t)\rangle)^{1/2}. \tag{16}$$

A simple analytic expression for $\langle\gamma_\perp(\phi_0,t)\rangle$ at saturation which will permit us to determine the maximum field strength through (16), is obtained in Section VI.

Since our system of fields and particles is independent of the spatial variable y, we note that the y component of canonical momentum $P_y = \gamma_\perp m_0 v_y - c^{-1}|e|A_y(x,t) - \Omega_0 m_0 x$ is a constant of the motion for each particle. The conservation of total energy as well as the y component of canonical angular momentum is monitored throughout the numerical simulations of (10) and (13) to ensure consistency.

The nonlinear model developed in this section is directly applicable to the experimental situation in which a wave is spatially amplified in the streaming direction of a gyrating beam. The saturation levels obtained with the present model are directly related to the saturation levels in an amplifier when the axial beam velocity equals the wave group velocity. As pointed out in Section III, this situation corresponds to a grazing intersection of the waveguide mode with the beam cyclotron mode when viewed on the dispersion diagram. Furthermore, such a grazing intersection leads to an absolute maximum in the temporal growth rate. In a steady-state amplifier the input wave amplitude initially grows exponentially, enters the nonlinear regime, and saturates. If we follow a group of particles contained in a thin cross-sectional slab of the beam, we note that the net flow of total energy flux into this slab is zero since we only consider the case where the axial beam velocity and wave group velocity are equal. Therefore, in the reference frame of the particles, the field amplitude evolves in time. This is precisely the situation described by our model. With the appropriate transformations (see Appendix B), the saturation levels of the spatially amplified wave can be obtained with the present temporal model.

V. Nature of Approximations

A number of approximations have been made in developing our nonlinear model. Among these are 1) the assumption of a single unstable wave, 2) the assumption of a single excited vacuum mode in the loaded guide and, finally, 3) the initially monoenergetic beam approximation. In this section the regimes of validity of these approximations are examined. We find that our model is valid for a wide range of parameters.

To verify the validity of the single wave approximation, the growth rate and field energy spectrum are examined. Using a Taylor series expansion of the linear growth rate about $k_0 = 0$, $\Gamma(k_0) \approx \Gamma(0) + (1/2)(\partial^2\Gamma(0)/\partial k_0{}^2)k_0{}^2$, we find that the half-width of the growth rate spectrum is $\Delta k = 2(\Gamma(0)/|\partial^2\Gamma(0)/\partial k_0{}^2|)^{1/2}$. Since the field energy is proportional to $\exp(2\Gamma(0)t)$, the half-width of the energy spectrum after the field has e folded N times, $t = N/\Gamma(0)$ is

$$\begin{aligned}\delta k &= 2(\ln 2/N)^{1/2}(\Gamma(0)/|\partial^2\Gamma(0)/\partial k_0{}^2|)^{1/2} \\ &= N^{-1/2}(\ln 2)^{1/2}\,\Delta k. \end{aligned} \tag{17}$$

From the linear dispersion relation (1), we find that, for the two cases discussed in Section III, the half-width of the linear growth rate spectrum for case 1) (i.e., $\beta_{0\perp} \gtrsim \beta_{\perp,\mathrm{crit}}$ and $\omega_0 = ck_n = l\Omega_0/\gamma_{0\perp}$) is

$$\Delta k_i \approx 2\sqrt{6}\,(\Gamma_i(0)/c)\left(\frac{\omega_0}{\Delta\omega_0}\right)^{1/2} \tag{18a}$$

and for case 2) (i.e., $\beta_{0\perp} \gg \beta_{\perp,\mathrm{crit}}$ and $\omega_0 = ck_n = l\Omega_0/\gamma_{0\perp}$), is

$$\Delta k_{ii} \approx \omega_0/c. \tag{18b}$$

In (18a), $\Gamma_i(0)$ is the linear growth rate at $k_0 = 0$ as given by (3b). The half-width of the energy spectrum after the field amplitude has e folded N times is for case 1)

$$\delta k_i \approx 2\sqrt{6}\,(\ln 2)^{1/2}N^{-1/2}(\Gamma_i(0)/\Delta\omega_0)\left(\frac{\Delta\omega_0}{\omega_0}\right)^{1/2}\omega_0/c \tag{19a}$$

and for case 2)

$$\delta k_{ii} \approx (\ln 2)^{1/2}N^{-1/2}\omega_0/c. \tag{19b}$$

The frequency spread corresponding to the wave number spread in (19a) and (19b) can be estimated from the vacuum dispersion relation $\omega = (\omega_0{}^2 + c^2k_0{}^2)^{1/2}$. The frequency spread is given approximately by $\delta\omega \approx (c\delta k/\omega_0)^2\omega_0$. From the expressions for the half-widths of the energy spectrum in (19a) and (19b) and the frequency spread, we see that the spectrum can be represented by a single wave if

$$N^{-1/2}(\Gamma_i(0)/\Delta\omega_0)(\Delta\omega_0/\omega_0)^{1/2} \ll 1$$

for case 1) and $N^{-1/2} \ll 1$ for case 2). Typically, in the examples we shall consider the number of e folds before the wave saturates is $N \approx 15$.

In the nonlinear analysis, the general form of the excited wave was that of a single vacuum waveguide mode. In the presence of a tenuous electron beam, this vacuum mode is expected to be a good representation of the actual field in the loaded guide. If the particle density is sufficiently large, the field induced by the beam current density will couple to more than one vacuum waveguide mode. Consequently, the profile of the actual field will differ from the form $\sin(k_n(x - a))$, used in the analysis. We now show that, in the tenuous beam limit, the correction to the vacuum waveguide field is of order $\Delta\omega/\omega_0$ and can, therefore, be neglected.

To obtain a rough estimate for the correction to the vacuum field, we assume that the particle current density at the frequency ω is produced solely by the vacuum mode given in (5). To simplify the calculation we take $x \ll a$. The electric field in the loaded waveguide is chosen to have the form

$$\begin{aligned}E_y(x,t) = &-E_0(t)\cos(\omega_0 t + \alpha(t)) \\ &\cdot \sum_{m=1}^{\infty} a_m \sin(k_m(x - a))\end{aligned} \tag{20}$$

where $E_0(t)$, ω_0, $\alpha(t)$, and k_m have been defined following (5), and a_m are the constant relative amplitude coefficients of the electric field. If corrections to the nth vacuum mode are desired, we assume that the current density is produced by the nth vacuum mode given in (5). Substituting the vector potential associated with (20) into the wave equation (7), we find

$$\begin{aligned}\sum_{m=1}^{\infty}\Big\{&[\omega_0{}^2 - c^2k_m{}^2 + (c^2k_m{}^2 + \omega_0{}^2)\dot\alpha/\omega_0]E_0(t)\sin(\omega_0 t + \alpha) \\ &- (c^2k_m{}^2 + \omega_0{}^2)(\dot E_0/\omega_0)\cos(\omega_0 t + \alpha)\Big\}\, a_m \sin(k_m(x - a)) \\ &= -4\pi\omega_0 J_y(x,t).\end{aligned} \tag{21}$$

The current density in (21) can now be written as

$$J_y(x,t) = \sum_{m=1}^{\infty} J_m(t) \sin k_m(x - a) \tag{22}$$

where

$$J_m(t) = \begin{cases} -(|e|\sigma_0/(2\pi a))(-1)^{(m+1)/2}\langle v_y(\phi_0,t)\rangle, & \text{for } m \text{ odd} \\ 0, & \text{otherwise} \end{cases}$$

when $k_m x(\phi_0,t) \ll \pi/2$. Combining (21) and (22) and neglecting higher order terms, we find

$$a_m \approx \frac{\omega_b{}^2}{4\gamma_{0\perp} D^2}\left(\frac{(1+\gamma_{0\perp}{}^2)}{\gamma_{0\perp}{}^2}\delta\omega - \beta_{0\perp}{}^2\frac{\Omega_0}{\gamma_{0\perp}}\frac{(\delta^2\omega - \Gamma^2)}{D^2}\right) \cdot (\omega^2 - c^2 k_m{}^2)^{-1} \tag{23}$$

where $m \neq n$ and the linear expression for $v_y(\phi_0,t)$ given by (A4) was used. Comparing the right-hand side of (23) with (A5a) shows that

$$a_m \approx \frac{((\omega_0{}^2 - c^2 k_n{}^2) + (\omega_0{}^2 + c^2 k_n{}^2)\,\Delta\omega/\omega)}{\omega_0{}^2 - c^2 k_m{}^2}$$

which reduces to

$$a_m \approx \frac{2(\Delta\omega/\omega_0)}{1 - (m/n)^2} \ll 1 \tag{24}$$

since $\omega_0 \approx ck_n$. The coupling to other vacuum waveguide mode is of order $\Delta\omega/\omega_0$, and hence our original choice for the electric field given in (5) is indeed reasonable.

In this paper we consider the beam to be initially monoenergetic in the beam frame. The range of validity of this assumption requires some examination. Since reference will be made to quantities in both the laboratory and beam frames, we shall denote the former with unprimed variables and the latter with primes. It is clear that the cold beam approximation will be valid if the total initial spread in $\gamma_\perp{}'$ satisfies $\delta\gamma_\perp{}' \ll 2(\gamma_{0\perp}{}' - \langle\gamma_\perp{}'\rangle_s)$, where $\langle\gamma_\perp{}'\rangle_s$ is the average value of γ at saturation. In terms of efficiency, this condition becomes

$$\delta\gamma_\perp{}'/\gamma_{0\perp}{}' \ll 2\eta'(\gamma_{0\perp}{}' - 1)/\gamma_{0\perp}{}' \tag{25}$$

where η' is the beam frame efficiency defined as $\eta' = (\gamma_{0\perp}{}' - \langle\gamma_\perp{}'\rangle_s)/(\gamma_{0\perp} - 1)$. Since the unstable wave has an infinite parallel wavelength in the beam frame, any spread in $v_\parallel{}'$ which does not violate the above inequality is unimportant.

To define the beam qualities necessary for the validity of our cold beam approximation, it is useful to express (25) in terms of laboratory frame quantities. The right-hand side of (25) can be written in terms of laboratory frame quantities by using the transformation rule for efficiency derived in Appendix B, i.e., $\eta = \eta'(\gamma_{0\perp}{}' - 1)\gamma_0/(\gamma_{0\perp}{}'(\gamma_0 - 1))$ where η is the power efficiency in the laboratory frame. Using the results of Appendix *B*, the inequality in (26) becomes

$$\delta\gamma_\perp{}'/\gamma_{0\perp}{}' \ll \frac{2(\gamma_0 - 1)}{\gamma_0}\eta \tag{26}$$

where $\gamma_0 = (1 - v_{0\parallel}{}^2/c^2 - v_{0\perp}{}^2/c^2)^{-1/2}$.

A spread in the beam frame gamma $\delta\gamma_\perp{}'$ can arise from a) a finite beam temperature in the laboratory frame or, in the case of a monoenergetic beam in the laboratory frame, b) a spread in the velocity space angle of the particles.

In case a) only a temperature spread in the perpendicular velocity is considered, so that $v_\perp = v_{0\perp} + \Delta v_\perp$ where $\Delta v_\perp \ll v_{0\perp}$ is the thermal component of velocity. Only perpendicular temperature is considered since a parallel temperature in the laboratory frame $\Delta v_\parallel$ contributes a higher order correction to $\delta\gamma_\perp{}'$ than $\Delta v_\perp$ if $\Delta v_\parallel$ and $\Delta v_\perp$ are of the same order. Since the perpendicular momentum is frame invariant, $\gamma v_\perp = \gamma_\perp{}' v_\perp{}'$, we find that the thermal spread in γ takes the form

$$\Delta\gamma = \pm\,\gamma_{0\parallel}\,\Delta\gamma_\perp{}' \tag{27}$$

where $\gamma_{0\parallel} = (1 - v_{0\parallel}{}^2/c^2)^{-1/2}$, $v_{0\parallel}$ is the axial laboratory frame velocity, and $\Delta\gamma_\perp{}' = 2(v_{0\perp}/c)\gamma_0{}^3\,\Delta v_\perp/c$ is the thermal spread in $\gamma_\perp{}'$ due to $\Delta v_\perp{}' = \gamma_{0\parallel}\,\Delta v_\perp$. Substituting (27) into (26) gives the following requirement for neglecting thermal effects in $v_\perp$:

$$\Delta\gamma/(\gamma_0 - 1) \ll 2\eta. \tag{28}$$

In the preceding inequality the efficiency η is calculated using the cold beam approximation.

In case b) the particles have the same energy; however, a spread in the velocity components exists. Consequently, the particle velocity components in the laboratory frame can be written as

$$v_\perp = v_{0\perp} - v_{0\perp}\,\Delta\theta \tag{29a}$$

$$v_\parallel = v_{0\parallel} + v_{0\perp}\,\Delta\theta \tag{29b}$$

where $|\Delta\theta| \ll 1$ is the spread of the velocity space angle, i.e., the angle between the total velocity vectors of the particles. To first order in $\Delta\theta$, we see that $v_\parallel{}^2 + v_\perp{}^2 = v_{0\parallel}{}^2 + v_{0\perp}{}^2$, so that the system of particles is monoenergetic in the laboratory frame. The transformation rule for γ from the laboratory to the beam frame $\gamma' = \gamma_{0\parallel}\gamma(1 - v_{0\parallel}v_\parallel/c^2)$ shows that the particles are not monoenergetic in the beam frame. In the beam frame we find that

$$\gamma_\perp{}' = \gamma_{0\perp}{}' + \Delta\gamma_\perp{}' \tag{30}$$

where $\gamma_{0\perp}{}' = \gamma_0/\gamma_{0\parallel}$ and $\Delta\gamma_\perp{}' = \gamma_{0\parallel}\gamma_0(v_{0\parallel}v_{0\perp}/c^2)\,\Delta\theta$. Substituting $\Delta\gamma_\perp{}'$ into (26) gives a condition on the magnitude of the maximum angular spread

$$|\Delta\theta|_{\max} \ll \frac{2(\gamma_0 - 1)}{\gamma_0}\frac{\eta}{\gamma_{0\parallel}{}^2 v_{0\parallel}v_{0\perp}/c^2} \tag{31}$$

allowed in the cold beam approximation. We will return to conditions (28) and (31) in the next section.

One of the causes of energy spread in an unneutralized beam is the self-electrostatic field. For the planar beam that we have considered, the total spread in $\gamma_\perp{}'$ can be shown to be

$$\delta\gamma_{\perp,\text{self}}' \approx (\mu')^2\beta_{0\perp}{}'((\Omega_0/\gamma_{0\perp}{}')/ck_n)\gamma_{0\perp}{}' \tag{32}$$

where $\mu' = \omega_b{}'/(\sqrt{\gamma_{0\perp}{}'}\,\omega_0{}')$ and $\omega_0{}' = \Omega_0/\gamma_{0\perp}{}'$. Considering (25), this imposes an upper limit on μ', and hence the beam current in the laboratory frame.

VI. Saturation Mechanisms

In this section some qualitative arguments concerning the saturation of the electron cyclotron maser instability are made. There are two mechanisms which are responsible for saturation of the unstable wave in the maser instability. They are 1) depletion of the rotational free energy of the electrons and 2) phase trapping of the gyrating particles in the wave. Which of the two mechanisms is actually responsible for saturation in a particular situation depends on the initial beam parameters.

Case 1): Free Energy Depletion

As mentioned in Section III, the linear dispersion relation [see (1)] gives rise to a threshold condition for instability given by $\beta_{0\perp} > \beta_{\perp,\text{crit}}$. That is, the maximum free energy per particle available to the wave is

$$\varepsilon_{\text{free}} = (\gamma_{0\perp} - \gamma_{\perp,\text{crit}})m_0c^2 \tag{33}$$

where $\gamma_{\perp,\text{crit}} = (1 - \beta_{\perp,\text{crit}}^2)^{-1/2}$. If the beam particles were to lose all of the free energy given by (32), the energy conversion efficiency would be

$$\eta = \frac{(\gamma_{0\perp} - \gamma_{\perp,\text{crit}})}{(\gamma_{0\perp} - 1)} \tag{34}$$

where $\gamma_{0\perp} \gtrsim \gamma_{\perp,\text{crit}}$. This, of course, is a rough approximation, since as the instability develops the particles warm up, while the threshold condition was obtained for a cold beam. Furthermore, as will be seen, competing processes such as electron trapping may take place before the beam loses its free energy. However, if $\gamma_{0\perp}$ is slightly greater than $\gamma_{\perp,\text{crit}}$, the expression in (33) will represent a good approximation to the actual conversion efficiency. Since, if $\gamma_{0\perp} \gtrsim \gamma_{\perp,\text{crit}}$, the particles lose all their free energy before thermalizing or trapping takes place and the wave will be linearly stabilized. If, however, $\gamma_{0\perp} \gg \gamma_{\perp,\text{crit}}$, the particles will phase trap in the wave and saturation will occur before all the free energy is used up.

Case 2): Phase Trapping

The condition for wave saturation due to phase trapping can be viewed in a number of ways. First, we have noted in Sections II and III that the frequency of the wave must be slightly greater than the relativistic electron cyclotron frequency $\Omega_0/\gamma_{0\perp}$ for an instability to develop. Therefore, initially we have

$$\omega - \Omega_0/\gamma_{0\perp} = \Delta\omega \gtrsim 0 \tag{35}$$

where $\Delta\omega$ is the frequency shift which can be obtained from the linear dispersion relation. Now, as the instability develops the average γ of the particles $\langle\gamma_\perp\rangle$ decreases until $\omega - \Omega_0/\langle\gamma_\perp\rangle = -\Delta\omega$. At saturation $\langle\gamma_\perp\rangle$ is minimum and

$$\omega - \Omega_0/\langle\gamma_\perp\rangle_s = -\Delta\omega \tag{36}$$

where $\langle\gamma_\perp\rangle_s$ is the average value of $\gamma_\perp$ at saturation. Comparing (35) with (36), we find that at saturation the average change in the γ of the particles $\langle\Delta\gamma_\perp\rangle_s = \gamma_{0\perp} - \langle\gamma_\perp\rangle_s$ is given by

$$\langle\Delta\gamma_\perp\rangle_s = 2\gamma_{0\perp}\,\Delta\omega/\omega. \tag{37}$$

The efficiency of conversion of kinetic energy to field energy η, when electron phase trapping is responsible for saturation, is

$$\eta = 2(\Delta\omega/\omega)\gamma_{0\perp}/(\gamma_{0\perp} - 1). \tag{38}$$

It should be noted that the efficiency in the beam frame cannot be made arbitrarily close to 100 percent simply by increasing the frequency shift $\Delta\omega$. The growth rate of the field is a function of $\Delta\omega$ and is nonvanishing for a limited range of $\Delta\omega$. The relations in (37) and (38) are valid only if $\Delta\omega$ lies within the nonvanishing part of the growth rate spectrum. To find the actual amplitude of the field at saturation $E_{0,s}$, we use the expression for conservation of total energy given in (16). The maximum field amplitude at saturation is easily shown to be

$$E_{0,s} = 4\,\frac{m_0c}{|e|}\,\omega_b(\gamma_{0\perp}\,\Delta\omega/\omega_0)^{1/2} \tag{39}$$

where it has been assumed that $\alpha/\omega_0 \ll 1$ and $ck_n/\omega_0 \approx 1$.

We now examine the nonlinear behavior of the particles with the aid of a constant of the motion derived from the orbit equations.

The orbit equations given in (13) can be written, in the small Larmor radius approximation $x \ll a$, as

$$\frac{du_\perp}{dt} = \frac{-|e|E_0}{m_0c}\cos((\omega_0 + \Delta\omega)t)\sin(\phi(t) + \phi_0) \tag{40a}$$

$$\frac{d\phi}{dt} = \frac{\Omega_0}{\gamma_\perp} - \frac{|e|E_0}{u_\perp m_0c}\cos((\omega_0 + \Delta\omega)t)\cos(\phi(t) + \phi_0) \tag{40b}$$

where $u_\perp = \gamma_\perp\beta_\perp$ is proportional to the transverse particle momentum, and $\gamma_\perp = (1 + u_\perp^2)^{1/2}$. The field amplitude E_0, as well as the frequency $\omega_0 + \Delta\omega$, are considered fixed and $\omega_0 = \Omega_0/\gamma_{0\perp}$ is the initial electron cyclotron frequency. The particle momentum $u_\perp m_0c$ and time rate of change of the velocity space angle $d\phi/dt$ consist of fast and slow time scale variations.

The fast time scale variation is associated with the wave frequency or electron cyclotron frequency, while the slow time scale is associated with the frequency shift $\Delta\omega$. The nonlinear behavior is governed predominantly by the slowly varying parts of $u_\perp$ and $d\phi/dt$. Since $(\omega_0 + \Delta\omega) - d\phi/dt$ changes slowly, the orbit equations in (40) written on the slow time scale become

$$\frac{du_\perp}{dt} = \frac{|e|E_0}{2m_0c}\sin(\lambda) \tag{41a}$$

$$\frac{d\lambda}{dt} = (\omega_0 + \Delta\omega) - \frac{\Omega_0}{\gamma_\perp} + \frac{|e|E_0}{2m_0cu_\perp}\cos(\lambda) \tag{41b}$$

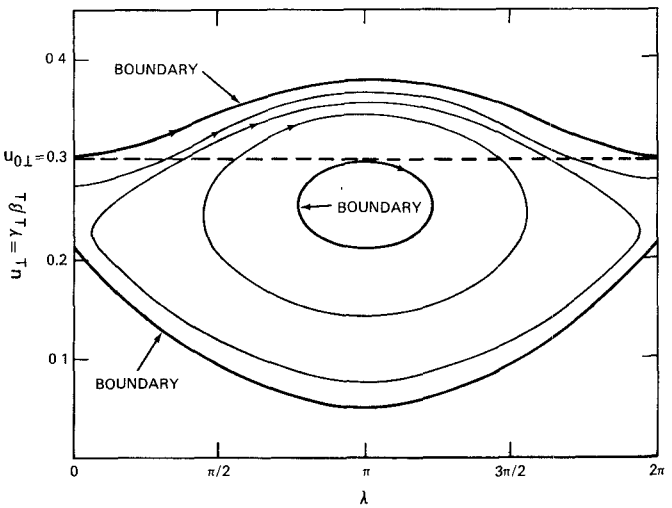

Fig. 6. Particle trajectories in velocity phase space as found from the constant of the motion. The figure shows the boundaries of the regions accessible to particles initially uniformly distributed between $0 \leq \lambda \leq 2\pi$ with $u_\perp = u_{0\perp}$.

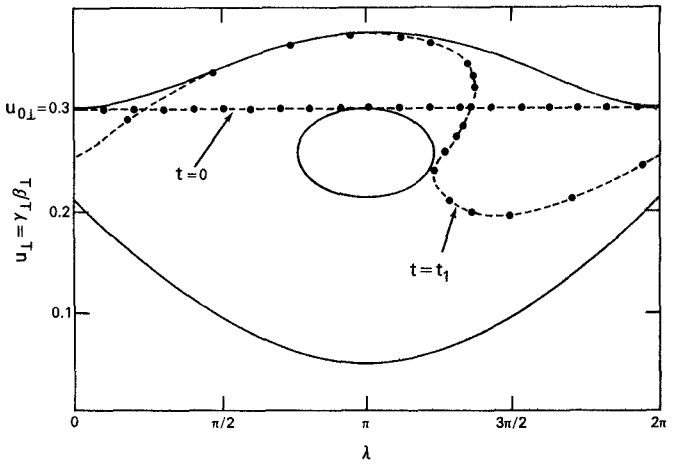

Fig. 7. The deformation of a monoenergetic beam in the presence of a constant amplitude field showing the actual particle positions in phase space. The curve for $t = t_0$ indicates the initial positions, and the one for $t = t_1$ the positions when the beam indicates trapping.

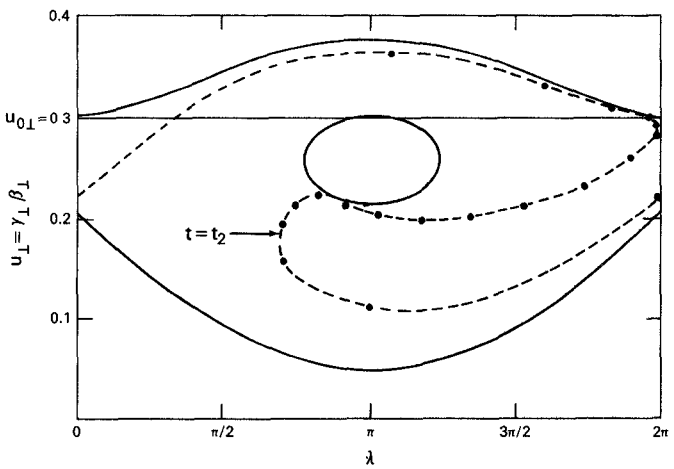

Fig. 8. The particle positions in phase space for a monoenergetic beam deformed by a constant amplitude electric field at $t = t_2$ when the particles have lost the maximum energy and are in a state corresponding to saturation.

where $\lambda = (\omega_0 + \Delta\omega)t - \phi(t) - \phi_0$. These slow time scale orbit equations have the following constant of motion:

$$C = \frac{|e|E_0}{m_0 c} u_\perp(t) \cos(\lambda(t)) + (\omega_0 + \Delta\omega) \cdot \left(\gamma_\perp(t) + \frac{\gamma_{0\perp}\omega_0}{\omega_0 + \Delta\omega}\right)^2. \quad (42)$$

Each particle moves in phase space $(u_\perp,\lambda)$ on C = constant curves. These C = constant curves describe the particle orbits when a constant frequency and constant amplitude field are instantaneously switched on. This situation can be realized by injecting particles into a field filled cavity. The particle trajectories in phase space lie on the constant C curves depicted in Fig. 6. The initial conditions for the example shown in the figure are $\gamma_{0\perp} = 1.05$, $\mu = 0.05$, $\Delta\omega/\omega_0 = 0.018$, and $|e|E_0/(\gamma_{0\perp}\omega_0 m_0 c) = 0.0025$. In this illustration the frequency shift is consistent with linear theory and the field amplitude E_0 corresponds to roughly a quarter of the value at saturation.

In Fig. 6 the particles are initially uniformly distributed between $0 \leq \lambda \leq 2\pi$ with $u_\perp = u_{0\perp}$. The trajectory followed by a particle is determined by its particular value of C which is different for each particle. The particles have access to a limited region of phase space, the boundaries of which are shown in Fig. 6. Particles which initially lie on closed C = constant curves are considered trapped even though $u_\perp$ as a function of λ is single valued. However, as the particles travel along their C = constant curve, $u_\perp$ will eventually become a multivalued function of λ. Similarly, for a growing field amplitude, particles can be considered trapped if they lie on closed C = constant curves, long before $u_\perp$ becomes a multivalued function of λ. The character of the accessible C = constant curves is determined, among other things, by the value chosen for E_0. For sufficiently small values of E_0, the particles will not lie on closed C = constant curves and, hence, are not trapped. The value of E_0 for which the first closed C = constant curve intersects the $u_\perp = u_{0\perp}$ line determines the field amplitude necessary for the onset of trapping. The separatix separating the closed and open orbits first intersects the line $u_\perp = u_{0\perp}$ at $\lambda = \pi$. As larger values of E_0 are chosen, the inaccessible interior region of phase space will contract and approach the point $u_\perp = u_{0\perp}$ and $\lambda = \pi$. At the value of E_0 for which the inaccessible interior region vanishes, the average particle energy ceases to decrease. The value of electric field amplitude necessary for the disappearance of the interior region is

$$E_0 \approx 2 \frac{m_0 c\omega_0}{|e|} u_{0\perp} \frac{\Delta\omega}{\omega_0}. \quad (43)$$

In Figs. 7 and 8 the actual positions of the particles in phase space are shown at various times. The parameters used for these figures are the same as those used in Fig. 6.

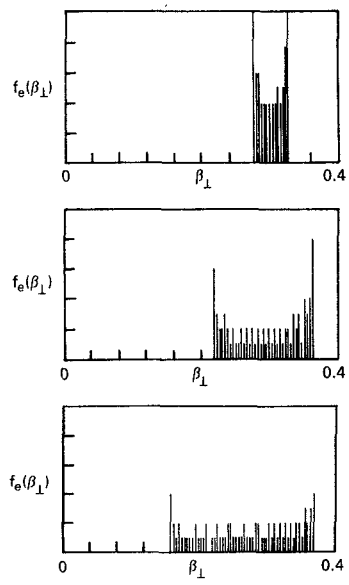

Fig. 9. The distribution functions of the electron beam deformed by a constant amplitude electric field at $t = t_0, t_1, t_2$.

Superimposed on the curves in Figs. 7 and 8 are the boundaries of the accessible region of the C = constant curves. At $t = 0$, when the electric field is switched on, the particles are uniformly distributed along the $u_\perp = u_{0\perp}$ line between $0 \leq \lambda \leq 2\pi$. In the constant amplitude electric field the particles proceed to bunch and rotate about the interior boundary as shown in the figures. At $t = t_1$ the particles begin to overtake each other and bunch along the right-hand side of the interior boundary. At a still later time $t = t_2$, the particles rotate and bunch along the bottom of the interior region. At this point the configuration corresponds to the saturation state since the average particle energy is at a minimum. The average kinetic energy continues to oscillate as the particles rotate about the interior boundary in a clockwise direction. The distribution functions $f_e(u_\perp)$ corresponding to the phase space trajectories in Figs. 7 and 8 are shown in Fig. 9. As can be seen from Figs. 8 and 9, not all the particles are located at the bottom of the interior boundary at saturation. Consequently, the average of $u_\perp$ at saturation is not exactly given by $u_\perp$ at the bottom of the interior region.

For sufficiently small values of E_0 the accessible C = constant curves are open and particles are not trapped. As E_0 is increased, the first particle to become trapped is always the one initially located at $(u_{0\perp},\pi)$. Trapping begins when the particle at $(u_{0\perp},\pi)$ has a closed orbit with turning points at $\lambda = 2\pi$ and 0. At these turning points, $d\lambda/dt$ vanishes. Since the constant C is invariant along this closed orbit and $d\lambda/dt$ vanishes at $\lambda = 2\pi$ and 0, we can obtain the threshold value of E_0 for trapping from (41b) and (42). The approximate value of the field amplitude for the onset of trapping is given by

$$E_0 = \frac{\omega_0 m_0 c}{4|e|u_{0\perp}} \gamma_{0\perp}^2 \left(\frac{\Delta\omega}{\omega_0}\right). \tag{44}$$

Using the constant of the motion in (42), the minimum value of $u_\perp$ reached by the first trapped particle occurs at $\lambda = \pi$ and is approximately

$$u_{\perp,\min} = u_{0\perp} - \frac{2\gamma_{0\perp}^2}{u_{0\perp}} \left(\frac{\Delta\omega}{\omega_0}\right). \tag{45}$$

The corresponding minimum γ for this particle is $\gamma_{\perp,\min} = \gamma_{0\perp} - 2\gamma_{0\perp}\,\Delta\omega_0/\omega_0$. Consequently, the first trapped particle undergoes a change in γ at $\lambda = \pi$ given by

$$\Delta\gamma_\perp = 2\gamma_{0\perp}\,\Delta\omega_0/\omega_0. \tag{46}$$

This expression for the maximum change in γ allows us to estimate the field amplitude at saturation as was done in (39). The change in γ given in (46) is identical to the value found in (37), where a different line of reasoning was used.

VII. Results

The nonlinear coupled equations (10a), (10b), (13a), and (13b) are solved numerically for a wide range of parameters. In each case the distribution function was represented by approximately 40–100 test particles. The actual number of particles used was determined by performing runs with larger and larger numbers of particles until no discernible difference appeared in the results. The conservation of both total system energy and canonical y momentum was monitored. The integration timesteps were adjusted to maintain the conservation of both constants to within 0.5 percent over the duration of a run. As diagnostic aids, plots of the test particle velocity distribution function, velocity space, and phase space were made at various times during the runs.

A run was initiated by uniformly distributing the particles in the velocity space angle $0 \leq \phi_0 \leq 2\pi$ and assigning them the same perpendicular velocity $v_\perp = v_{0\perp}$. A small amplitude electric field was introduced as a perturbation and allowed to grow self-consistently. From the results of the single wave simulation runs, we have made composite graphs of the transfer efficiency from particle kinetic energy to wave electromagnetic energy at saturation as a function of several parameters. A comparison between these results and the analytic predictions in Section VI shows good qualitative agreement.

We will now discuss the phase space dynamics for the two saturation mechanisms discussed in Section VI. The evolution of the particles in phase space and their distribution functions is shown when saturation occurs by 1) free energy depletion and 2) phase trapping. In the free energy depletion case the initial parameters are $\gamma_{0\perp} = 1.012 \gtrsim \gamma_{\perp,\text{crit}} = 1.0108$, $\mu = 0.05$, where μ is a dimensionless parameter related to the beam density through $\mu = \omega_b/(\sqrt{\gamma_{0\perp}}\,\omega_0)$, $\omega_0 = ck_n = l\Omega_0/\gamma_{0\perp}$, and $l = n = 1$. Fig. 10(a) and (b) shows the particle phase space in the course of the instability when the growth is still linear. At saturation, shown in Fig. 10(c), the particles indicate no phase trapping. The average particle $\gamma_\perp$ at saturation is within a few percent of $\gamma_{\perp,\text{crit}}$. However, the individual particles energies have a large variation, as can be seen from the distribution functions depicted in Fig. 11(b) and (c). The

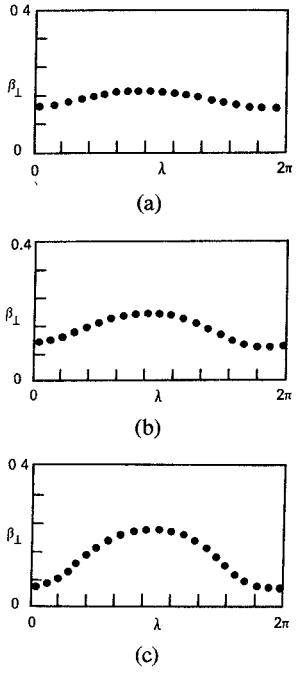

Fig. 10. The particle positions in phase space from a simulation of the cyclotron maser instability in the case of saturation by energy depletion. (a) $t = t_1$, linear phase. (b) $t = t_2$, nonlinear phase. (c) $t = t_3$, at saturation.

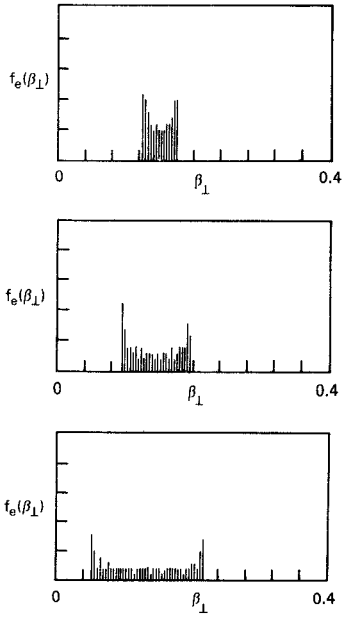

Fig. 11. The distribution function of the electrons from a case of saturation by energy depletion at various times as in Fig. 10.

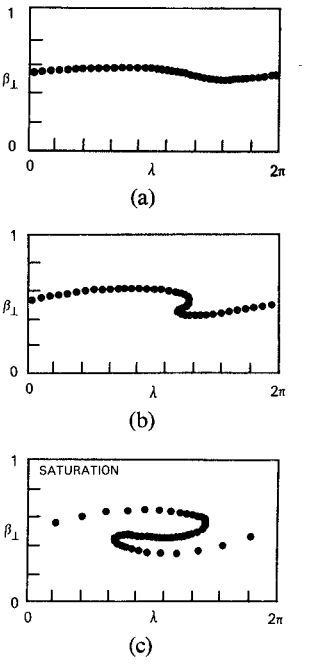

Fig. 12. Particle positions in phase space from a simulation in the case of saturation by trapping. (a) Linear phase. (b) Nonlinear phase. (c) At saturation.

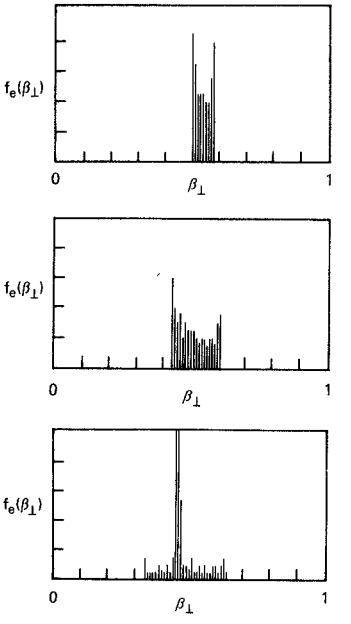

Fig. 13. The distribution function for saturation by trapping for times given in Fig. 12.

predicted efficiency according to (34) is $\eta = (\gamma_{0\perp} - \gamma_{\perp,\mathrm{crit}})/(\gamma_{0\perp} - 1) \approx 10$ percent. This is in excellent agreement with the numerically evaluated efficiency of 10 percent. To illustrate case 2), where phase space trapping is responsible for saturation, we choose the parameters $\gamma_{0\perp} = 1.2$, $\mu = 0.05$. [Note that $\gamma_{\perp,\mathrm{crit}} = 1.01$ for this case as in case 1).] The particle dynamics in velocity phase space and the velocity distribution function are shown at various times τ during the evolution of the run in Figs. 12 and 13. In Fig. 12(a) the particles are shown at $\tau = 250$ when they have begun to display some bunching but are relatively close to their initial phase space positions. The corresponding distribution function in Fig. 13(a) displays little spread in velocity. When the nonlinear effects manifest themselves by a change in the growth rate, the velocity phase space bunching becomes distinctly visible and the velocity distribution begins to spread as shown in Figs. 12(b) and 13(b). In Figs. 12(c) and 13(c), we show the velocity phase space and distribution function at saturation. The phase space plots in Figs. 12(b) and 12(c) show the trapped electrons circulating and forming a tongue

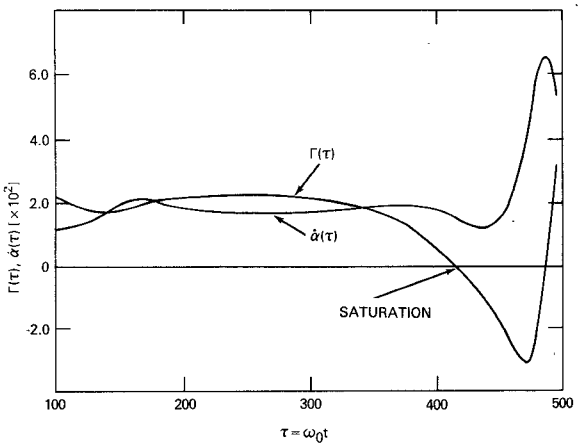

Fig. 14. The nonlinear phase shift and growth rate as a function of time for a typical simulation.

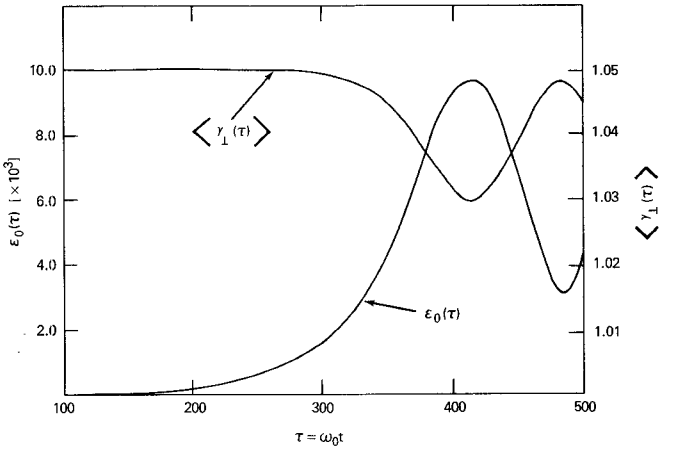

Fig. 15. The field amplitude and average beam γ as a function of time for a typical simulation.

configuration, similar to the one in Figs. 7 and 8, where a constant electric field was present. The saturation mechanism for this case is clearly phase trapping of the beam electrons in the wave. Because not all the electrons are trapped, an average over the distribution function is necessary to determine $\langle\gamma_\perp\rangle_s$. This necessitates the introduction of a numerical factor f in the simple expression corresponding to (37):

$$\langle\Delta\gamma_\perp\rangle_s/\gamma_{0\perp} = 2f\,\Delta\omega/\omega_0.$$

The factor f is a number on the order of unity and depends on the fraction of deeply trapped particles $f \lesssim 1$.

As an example of a typical run, we shall follow the evolution of field and particle quantities as a function of time. The initial conditions chosen for this example are: $\mu = 0.05$, $\gamma_{0\perp} = 1.05$, $\omega_0 = ck_n = \Omega_0/\gamma_{0\perp}$ and $n = 1$, and $\mu = \omega_b/(\sqrt{\gamma_{0\perp}}\,\omega_0)$. In Fig. 14, the nonlinear frequency shift and growth rate are shown as functions of the normalized time parameter $\tau = \omega_0 t$. Initially, for $\tau \lesssim 150$ when the field amplitude is small, we see a transient, during which the perturbing field comes into equilibrium with the particles. That is, initially the presence of the small amplitude electric field is inconsistent with the initial conditions of the beam particles. During the early transient

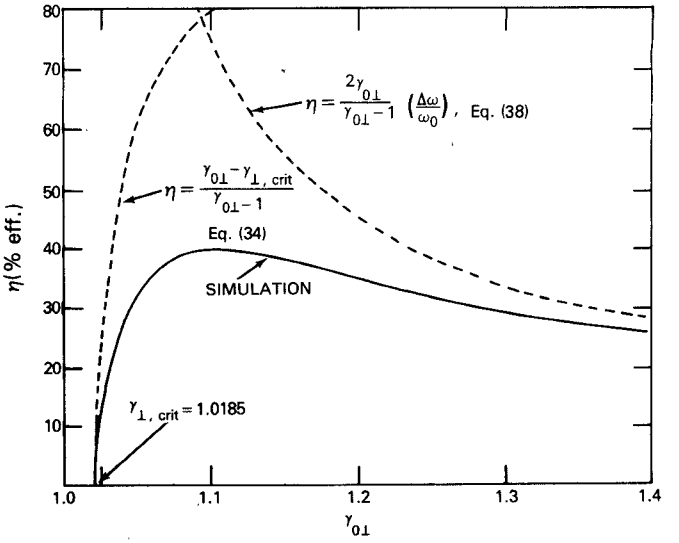

Fig. 16. The efficiency of the cyclotron maser as a function of energy found from the two mechanisms of saturation and from simulations.

the field and particles adjust themselves to self-consistently satisfy (10a), (10b), (13a), and (13b). The transient regime lasts for a time roughly given by $\tau_{tran} \approx \omega_0/\Gamma_L$. The linear regime $150 \lesssim \tau \lesssim 350$ follows the initial transient. In this regime the wave grows exponentially and both the growth rate and frequency shift assume the values predicted by linear theory. As will be apparent from one of our later figures, the growth rates and frequency shifts in the linear regime are in excellent agreement with those found from the linear dispersion relation. The exponentially growing wave attains a sufficiently high amplitude by $\tau = 350$ to start nonlinearly affecting the particle dynamics, and the growth rate begins to decrease until it reaches zero at $\tau \approx 420$ when saturation occurs.

The nonlinear change in the growth rate is accompanied by a less pronounced change in the frequency shift prior to saturation. We find that for the parameters used in this example at saturation, $\omega_0 + \dot{\alpha}(\tau) - \Omega_0/\langle\gamma_\perp\rangle \approx 0$ in good agreement with the qualitative argument in Section VI. The normalized field amplitude, $\varepsilon_0(\tau) = |e|E_0(\tau)/(m_0c\omega_0)$, and the average perpendicular particle energy $\langle\gamma_\perp\rangle$ are shown as functions of τ in Fig. 15.

We have found that the energy efficiency curves for a given set of parameters always display a maximum. For example, with $\mu = 0.1$, the efficiency curve shown in Fig. 16 has a peak of 40 percent when $\gamma_{0\perp} = 1.1$. The peak results from the competition between the two saturation mechanisms described in Section VI. As can be seen in Fig. 16, the efficiency curve has a cutoff at $\gamma_\perp = \gamma_{\perp,crit} = 1.0185$. The curves of the linear growth rates and frequency shifts, obtained by numerically solving the linear dispersion relation of (1) are shown in Fig. 17 as a function of $\gamma_{0\perp}$. The linear growth rate curve shows a threshold at $\gamma_{0\perp} = 1.0185$, identical to that in Fig. 17. Fig. 17 also shows a comparison between the results of linear theory [see (1)], and of the particle simulations in the linear regime. Clearly, the linear growth rates and frequency shifts are in excellent agreement. For beams that have initial energies characterized by

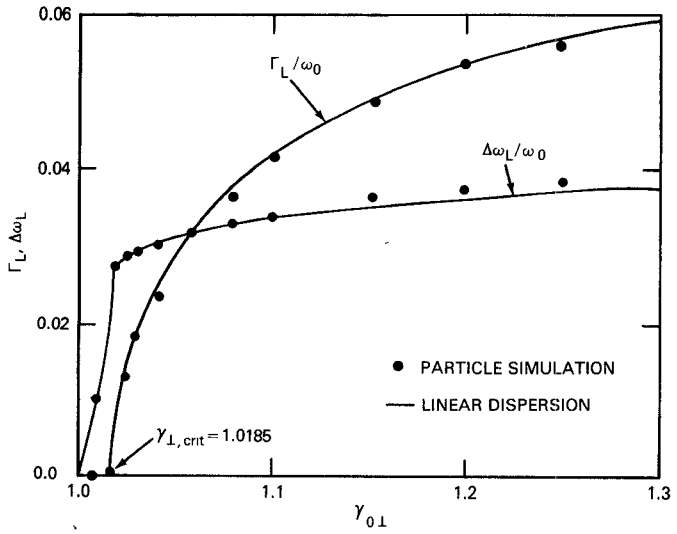

Fig. 17. A comparison of the growth rate and phase shift predicted by linear theory and the results from the linear portions of the computer simulations.

$\gamma_{0\perp} \gtrsim \gamma_{\perp,crit}$, we find that the excited wave extracts free energy from the beam until $\langle\gamma_\perp\rangle = \gamma_{\perp,crit}$ and the system becomes linearly stable without particle trapping taking place. The simulations confirm this, since the velocity phase space plots show no evidence of trapping at the time of saturation when $\gamma_{0\perp} \gtrsim \gamma_{\perp,crit}$. In this regime a rough expression for the average change in $\gamma_\perp$ at saturation is

$$\langle\Delta\gamma_\perp\rangle_s = \gamma_{0\perp} - \gamma_{\perp,crit}$$

and implies an efficiency monotomically increasing with $\gamma_{0\perp}$; this is shown as a dashed curve on Fig. 16. In the other regime where $\gamma_{0\perp} \gg \gamma_{\perp,crit}$, the saturation mechanism is dominated by particle trapping and we find that $\langle\Delta\gamma_\perp\rangle_s = 2f\gamma_{0\perp}\,\Delta\omega/\omega_0$. This implies an efficiency curve monotomically decreasing with $\gamma_{0\perp}$ as shown in Fig. 16 with $f = 1$. The two saturation mechanisms described here predict an efficiency maximum; this is also verified by the results of the particle simulations.

Our saturation arguments show qualitative agreement with the actual efficiency obtained numerically. In the $\gamma_{0\perp} \gg \gamma_{\perp,crit}$ regime we have arbitrarily set $f = 1$, implying that all the particles are deeply trapped at saturation. From Fig. 16 we see that in the intermediate regime f is closer to 1/2. Similar arguments hold in the $\gamma_{0\perp} \gtrsim \gamma_{\perp,crit}$ regime. The dashed curves in Fig. 16 show the competition between two mechanisms leading to a maximum in the efficiency curves.

We now present the results of our nonlinear analysis for a wide range of parameters. In Fig. 18, energy efficiency as a function of $\gamma_{0\perp}$ is shown for various values of μ, μ = 0.025, 0.05, 0.15, and 0.35. In this figure the initial wave frequency ω_0 was set equal to ck_n with $n = 1$. Furthermore, the initial relativistic cyclotron frequency $\Omega_0/\gamma_{0\perp}$ was set equal to ck_n. These initial conditions on ω_0, ck_n, and $\Omega_0/\gamma_{0\perp}$ were selected because they occur near the maximum linear growth rate. All of the curves in Fig. 18 display a maximum in efficiency in the beam frame as a function $\gamma_{0\perp}$. This characteristic of the curves has already been explained.

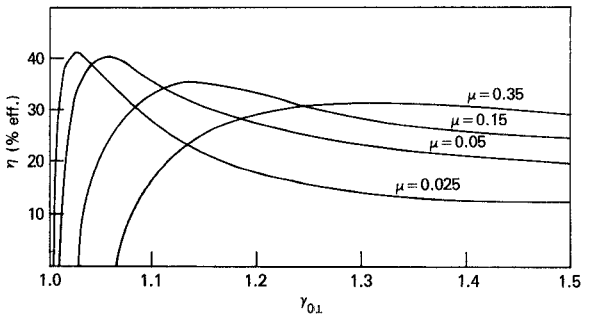

Fig. 18. The beam frame efficiency of the electron cyclotron maser as a function of energy for various densities when $ck_n = \Omega_0/\pi_{0\perp}$.

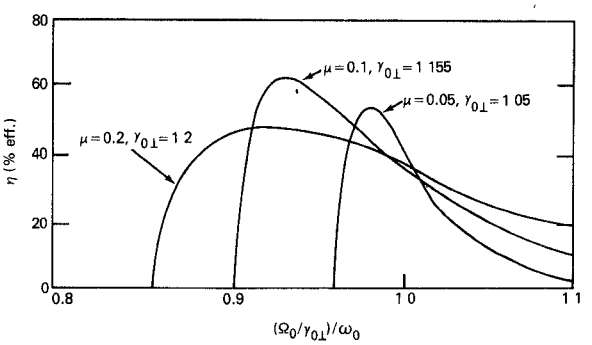

Fig. 19. The beam frame efficiency of the electron cyclotron maser when the cyclotron frequency is varied.

A further feature of the curves is that as μ increases, $\gamma_{\perp,crit}$ increases in agreement with the definition of $\beta_{\perp,crit}$ given in Section III. From Fig. 18 we also note that the efficiency increases at low values of $\gamma_{0\perp}$ as μ is decreased. This property of the curves can be explained by noting that as μ decreases, $\gamma_{\perp,crit}$ decreases, resulting in a sharp increase in efficiency as a function of $\gamma_{0\perp}$ near $\gamma_{\perp,crit}$. The maximum efficiency seems to level off at $\sim$40 percent for low values of $\gamma_{0\perp}$, when $\omega_0 = ck_n = \Omega_0/\gamma_{0\perp}$.

Dramatic increases in the efficiency can be realized in a number of ways. For example, by slightly mistuning the relativistic cyclotron frequency away from $\omega_0 = ck_n$, electron phase trapping can be postponed and higher efficiencies realized. In the regime where electron trapping is responsible for saturation, we have shown that the efficiency is roughly $2f\gamma_{0\perp}(\omega_0 + \Delta\omega - \Omega_0/\gamma_{0\perp})/(\gamma_{0\perp} - 1)$. By choosing $\omega_0 > \Omega_0/\gamma_{0\perp}$, we can expect the efficiency to increase. In Fig. 19 the efficiency is shown as a function of $(\Omega_0/\gamma_{0\perp})/\omega_0$ for various values of μ and $\gamma_{0\perp}$. The values for μ and $\gamma_{0\perp}$ were taken from the maximum efficiency points in Fig. 18. Fig. 19 shows clearly that higher efficiencies can be realized for $(\Omega_0/\gamma_{0\perp})/\omega_0$ less than unity. Since sufficiently small values of $(\Omega_0/\gamma_{0\perp})/\omega_0$ lie outside the growth rate spectrum, the efficiency drops to zero. By mistuning the magnetic field, the efficiency was increased from 40 to 63 percent in the beam frame for the case $\mu = 0.1$ and $\gamma_{0\perp} = 1.155$.

The efficiency can also be increased by varying the external magnetic field in time in such a way that $\omega - \Omega_0(\tau)/\langle\gamma_\perp(\tau)\rangle$ is held fixed. This procedure is similar to the mistuning

approach discussed, in that electron phase trapping is postponed. Choosing $\mu = 0.1$, $\gamma_{0\perp} = 1.1$, and changing the magnetic field in time such that $(\omega - \Omega_0(\tau)/\langle\gamma_\perp(\tau)\rangle)$ is fixed at its initial value of 0.034, an efficiency of ≈ 70 percent was realized. This compares with an efficiency of ≈ 40 percent when the magnetic field was held fixed at $\Omega_0/\gamma_{0\perp} = \omega_0 = ck_n$.

VIII. Discussion and Example

We have shown that the electron cyclotron maser mechanism can be an efficient method of producing short wavelength radiation. The mechanism seems particularly attractive for the generation of submillimeter radiation when higher cyclotron harmonics are considered. Preliminary results at high cyclotron harmonics and also higher waveguide modes indicate that the efficiency remains relatively high. These results, on the higher harmonics, will be published in a forthcoming paper.

Experiments on the cyclotron maser using intense relativistic electron beams[10-13] have produced efficiencies of less than 2 percent. The low experimental efficiencies are in good agreement with our theoretical results and are the result of the following. 1) The transformation of efficiency factor from the beam frame to the laboratory frame, i.e., $\gamma_0(\gamma_{0\perp}' - 1)/(\gamma_{0\perp}'(\gamma_0 - 1))$ [see (B7)], was typically small, <0.3. 2) The value of $\gamma_{0\perp}$ in the beam frame was not optimized for maximum efficiency (see Fig. 18). 3) The method used to produce transverse energy also introduced temperature in the beam distribution [see (28), (31), and (32)]. The combination of these effects led to the low observed efficiencies. With our improved understanding of the saturation levels and mechanisms, efficiencies can be substantially improved.

As an illustration of the beam and waveguide parameters needed to generate electromagnetic radiation at 1.0 cm, we consider the following detailed example. Referring to Fig. 2, we choose $a = 0.25$ cm and $L = 2\pi(2a) = 3.14$ cm. The waveguide width L corresponds to the circumference of a cylindrical guide having a radius equal to $2a$. In the laboratory frame we have a cold electron beam with a total energy of $V = 300$ keV per particle. The electron velocity is partitioned such that $v_{0\parallel} = 0.69c$ and $v_{0\perp} = 0.36c$. Therefore, the total γ of the beam electrons is

$$\gamma_0 = (1 - (v_{0\parallel}/c)^2 - (v_{0\perp}/c)^2)^{-1/2} = 1.59$$

and

$$\gamma_{0\parallel} = (1 - (v_{0\parallel}/c)^2)^{-1/2} = 1.37.$$

With a magnetic field $B_0 = 11.4$ kG, the electron Larmor radius is $r_L = v_{0\perp}/(|e|B_0/\gamma_0 m_0 c) = 0.34\,a = 0.085$ cm. Taking the axial current to be $I = 860$ A, with the beam thickness equal to twice the Larmor radius and beamwidth equal to L, we obtain a beam density in the laboratory frame of $n_e = I/(|e|v_{0\parallel}(2r_L L)) = 2.6 \times 10^{11}$ cm^{-3}. The electron surface density is given by $\sigma_0 = n_e(2r_L) = 4.42 \times 10^{10}$ cm^{-2}.

Now in the beam frame, $v_{0\parallel}' = 0$, hence, $\gamma_{0\perp}' = (1 - (v_{0\perp}'/c)^2)^{-1/2} = \gamma_0/\gamma_{0\parallel} = 1.155$ and $v_{0\perp}' = (1 - (\gamma_{0\perp}')^{-2})^{1/2} = 0.5c$. The electron surface density in the beam frame becomes $\sigma_0' = \sigma_0\gamma_{0\perp}'/\gamma_0 = 3.2 \times 10^{10}$ cm^{-2}, which determines the modified plasma frequency $\omega_b' = (4\pi|e|^2\sigma_0'/(m_0 a))^{1/2} = 2.02 \times 10^{10}$ s^{-1}. To obtain the efficiency in the beam frame η', we need μ' as well as $(\Omega_0/\gamma_{0\perp}')/(ck_n)$. To continue, we find that $\Omega_0/\gamma_{0\perp}' = |e|B_0/(\gamma_{0\perp}' m_0 c) = 1.75 \times 10^{11}$ s^{-1}, $ck_n = 1.88 \times 10^{11}$ s^{-1} and $(\Omega_0/\gamma_{0\perp}')/(ck_n) = 0.93$. Now $\mu' = (\omega_b'/\sqrt{\gamma_{0\perp}'})/\omega_0' = 0.1$, since ω_0' is set equal to the cutoff frequency ck_n. From Fig. 14 we find that for $\mu' = 0.1$, $\gamma_{0\perp}' = 1.155$, and $(\Omega_0/\gamma_{0\perp}')/\omega_0' = 0.93$ the efficiency in the beam frame is $\eta' = 63$ percent. Using (B7) of Appendix B, the efficiency in the laboratory frame is $\eta = \eta'\gamma_0(\gamma_{0\perp}' - 1)/(\gamma_0'(\gamma_0 - 1)) = 22$ percent. Since the beam power in the laboratory frame is $P_b = IV = 258$ MW, the radiated power becomes $P_r = \eta P_b = 57$ MW. The spread in $\gamma_\perp'$ in the beam frame due to the self-electrostatic fields can be estimated from (32). We find from (32) that $\delta\gamma_{\perp,\text{self}}'/\gamma_{0\perp}' = 0.0036$. From (25) we see that the initial spread in $\gamma_\perp'$ can be neglected if it satisfies the following requirement, $\delta\gamma_\perp'/\gamma_{0\perp}' \ll 2\eta'(\gamma_{0\perp}' - 1)\gamma_{0\perp}' = 0.17$. Clearly, in this example, the spread in $\gamma_\perp'$ due to self-fields can be neglected.

The possibility of high efficiency and power levels at millimeter and submillimeter wavelengths with the electron cyclotron maser makes it an attractive device for plasma heating. The frequencies required for heating at either the electron cyclotron or upper hybrid frequency are in excess of 120 GHz ($\lambda = 2.5$ mm) for reactor-type Tokomaks [28]. The cyclotron maser appears to be the only viable source for producing the required power efficiently at such high frequencies. Plasma heating using cyclotron maser devices has been demonstrated in the USSR on the TM-3 Tokomak [29]. In these experiments the electron cyclotron resonance at $\lambda = 5$ mm was used. It has been estimated that an experimental power reactor would require ~ 100–250 MJ of supplemental heating in 2–6 s [30]. This is a continuous wave requirement of $\lesssim 50$ MW at a frequency of 280 GHz ($\lambda = 1.07$ mm), assuming electron cyclotron heating and the reactor parameters of [30]. On a large device these requirements may be achieved by employing several maser devices simultaneously.

Appendix A

The linear dispersion relation can be recovered from the self-consistent nonlinear equations derived in Section III [see (1) and (13)]. To facilitate the calculation, we take the limit where the Larmor radius of the electrons is small compared to the characteristic transverse scale length over which the fields vary, $nx \ll a$. In this approximation the fields take the simplified form $E_y = E_0(t)\cos(\omega_0 t + \alpha(t))$ and $B_z = 0$, where the x dependence has been removed because in the small Larmor radius limit, $k_n(x - a) \approx nx/a$. In the linear approximation the magnitude of the particle velocity $\beta_\perp(t)$ and rotational frequency $\psi(t)$ are expanded as

$$\beta_\perp(t) = \beta_{0\perp} + \beta_\perp^{(1)}(t)$$
$$\psi(t) = \Omega_0/\gamma_{0\perp} + \psi^{(1)}(t) \qquad \text{(A1)}$$

where $\beta_\perp^{(1)} \ll \beta_{0\perp}$ and $\psi^{(1)} \ll \Omega_0/\gamma_{0\perp}$ are slowly varying functions of time and are linear in the wave amplitude $E_0(t)$. In this regime it is appropriate to set $E_0(t) = \varepsilon_0$

exp $(\Gamma_L t)$ and $\alpha(t) = \Delta\omega_L t$ where $\Gamma_L \ll \omega_0$ is the linear growth rate and $\Delta\omega_L \ll \omega_0$ is the linear frequency shift. Substituting (A1) into the orbit equations (13), we obtain the following slow time scale equations:

$$\dot{\beta}_\perp^{(1)}(t) = \frac{|e|\varepsilon_0 e^{\Gamma_L t}}{2\gamma_{0\perp}{}^3 m_0 c} \sin(\delta\omega t + \phi_0) \tag{A2}$$

$$\psi^{(1)}(t) = -\frac{\Omega_0}{\gamma_{0\perp}} \beta_{0\perp}\gamma_{0\perp}{}^2 \beta_\perp^{(1)}(t) - \frac{|e|\varepsilon_0 e^{\Gamma_L t}}{2\beta_{0\perp}\gamma_{0\perp} m_0 c} \cos(\delta\omega t + \phi_0) \tag{A3}$$

where $\delta\omega = \omega_0 - \Omega_0/\gamma_{0\perp} + \Delta\omega_L$. In (A3) the approximation $\gamma_\perp(t) \approx \gamma_{0\perp} + \beta_{0\perp}\gamma_{0\perp}{}^3\beta_\perp^{(1)}(t)$ is used. The linearized expression for the y component of particle velocity is

$$v_y(t) = c\beta_{0\perp} \sin\left(\frac{\Omega_0}{\gamma_{0\perp}} t + \phi_0\right) + c\beta_\perp^{(1)}(t) \sin\left(\frac{\Omega_0}{\gamma_{0\perp}} t + \phi_0\right) + c\beta_{0\perp} \int_0^t \psi^{(1)}(t')\, dt' \cos\left(\frac{\Omega_0}{\gamma_{0\perp}} t + \phi_0\right).$$

Solving (A2) and (A3) for times much longer than a growth time, $t \gg 1/\Gamma_L$ yields

$$v_y(t) = c\beta_{0\perp} \sin\left(\frac{\Omega_0}{\gamma_{0\perp}} t + \phi_0\right) - \frac{|e|\varepsilon_0 e^{\Gamma_L t}}{4\gamma_{0\perp} m_0 D^2} \cdot \left\{\left(\frac{(1+\gamma_{0\perp}{}^2)}{\gamma_{0\perp}{}^2}\Gamma_L - 2\beta_{0\perp}{}^2 \frac{\Omega_0}{\gamma_{0\perp}} \frac{\delta\omega\Gamma_L}{D^2}\right) \cos\tilde{\omega}t + \left(\frac{(1+\gamma_{0\perp}{}^2)}{\gamma_{0\perp}{}^2}\delta\omega - \beta_{0\perp}{}^2 \frac{\Omega_0}{\gamma_{0\perp}} \frac{(\delta\omega^2 - \Gamma_L{}^2)}{D^2}\right) \sin\tilde{\omega}t\right\} \tag{A4}$$

where $\tilde{\omega} = \omega_0 + \Delta\omega_L$, $D^2 = \delta\omega^2 + \Gamma_L{}^2$ and $\int_0^t \psi^{(1)}(t')\, dt' \ll 1$. The equations governing the frequency shift and growth rate [see (10a) and (10b)] in the linear approximation become

$$(\omega_0{}^2 - c^2 k_n{}^2 + 2\omega_0 \Delta\omega_L)\varepsilon_0 \exp(\Gamma_L t) = -\frac{2|e|\sigma_0}{\pi a} \omega_0\tilde{\omega} \cdot \int_t^{t+2\pi/\tilde{\omega}} dt' \int_0^{2\pi} d\phi_0 v_y(\phi_0, t') \sin\tilde{\omega}t' \tag{A5a}$$

$$\omega_0\Gamma_L\varepsilon_0 \exp(\Gamma_L t) = \frac{|e|\sigma_0}{\pi a} \omega_0\tilde{\omega} \cdot \int_t^{t+2\pi/\tilde{\omega}} dt' \int_0^{2\pi} d\phi_0 v_y(\phi_0, t') \cos\tilde{\omega}t' \tag{A5b}$$

where $v_y(\phi_0, t)$ is given by (A4). Since $\Delta\omega_L/\omega_0$, $\Gamma_L/\omega_0 \ll 1$ and $\omega_0 \approx ck_n$, we approximate $\omega_0{}^2 + c^2 k_n{}^2$ by $2\omega_0{}^2$ on the right-hand side of (A5). By multiplying (A5b) by $\sqrt{-1}$, adding it to (A5a), and performing the integrals over t' and ϕ_0, we arrive at the linear dispersion relation

$$(\omega^2 - c^2 k_n{}^2) = \frac{\omega_b{}^2 \omega}{2\gamma_{0\perp}} \cdot \left(\frac{1}{(\omega - \Omega_0/\gamma_{0\perp})} - \frac{\beta_{0\perp}{}^2}{2} \frac{\omega}{(\omega - \Omega_0/\gamma_{0\perp})^2}\right) \tag{A6}$$

where $\omega = \omega_0 + \Delta\omega_L + i\Gamma_L$. This result is identical to the dispersion relation given by (1) for waves of zero wave number, when $v_{0\perp} \ll (a\Omega_0/\gamma_{0\perp})/n$.

Appendix B

One of the objectives of this paper is to determine the efficiency of electromagnetic energy flux radiated by a beam undergoing the electron cyclotron maser instability. The general law governing the laboratory frame efficiency of conversion of beam to electromagnetic power in terms of beam frame energy efficiency is derived.

The analysis in the body of the text has been performed in a rather special frame in which beam axial velocity $v_{0\|}$ and wave group velocity v_g both vanish. The justification for choosing this frame is that the growth rate maximizes when $v_{0\|} = v_g$; therefore, by transforming to the beam frame, the axial beam velocity and the wave group velocity vanish simultaneously. In the beam frame the wave is at cutoff having an infinite axial wavelength $k_0 = 0$. In what follows the two frames are distinguished by denoting beam frame variables by primed quantities and laboratory variables by unprimed quantities. The notation in this Appendix should not be confused with that in the text where unprimed quantities refer to the beam frame.

In the laboratory frame the axial electromagnetic energy flux density $S_z = (c/4\pi)(\boldsymbol{E} \times \boldsymbol{B}) \cdot \hat{e}_z$ is found by a Lorentz transformation of the beam frame fields [derivable from (6)] and takes the form

$$S_z = \frac{c}{4\pi} \gamma_{0\|}{}^2 \beta_{0\|} (E_0'(t) \cos(\omega_0' t + \alpha') \sin k_n(x - a))^2 \tag{B1}$$

where $\beta_{0\|} = v_{0\|}/c$, $v_{0\|}$ is the axial beam velocity in the laboratory frame and $\gamma_{0\|} = (1 - \beta_{0\|}{}^2)^{-1/2}$. Using (B1), the temporal and spatial average of the electromagnetic power in the laboratory frame, flowing normal to the cross-sectional area $2aL$, is

$$P_f = \frac{c}{8\pi} \gamma_{0\|}{}^2 \beta_{0\|} (E_0')^2 aL \tag{B2}$$

where L is the length of the waveguide as shown in Fig. 2. From conservation of field and particle energy [see (16)], we obtain an expression for the maximum electric field, occurring at saturation, in the beam frame:

$$E_{0,s}' = \sqrt{2}\, B_0 \mu' (\omega_0'/(\Omega_0'/\gamma_{0\perp}'))^{1/2} \cdot (\gamma_{0\perp} - \langle\gamma_\perp'\rangle_s)^{1/2} (\gamma_{0\perp}')^{-1/2}. \tag{B3}$$

Expressing the electric field amplitude at saturation [see (B3)] in terms of the beam frame energy efficiency, $\eta' = (\gamma_{0\perp}' - \langle\gamma_\perp'\rangle_s)/(\gamma_{0\perp}' - 1)$, and substituting it into (B2) gives for the radiated power in the laboratory frame

$$P_f = \frac{c}{4\pi} \gamma_{0\|}{}^2 \beta_{0\|} B_0{}^2 (\mu')^2 \frac{\omega_0'}{\Omega_0'/\gamma_{0\perp}'} \frac{(\gamma_{0\perp}' - 1)}{\gamma_{0\perp}'} aL\eta'. \tag{B4}$$

The efficiency of conversion of beam to electromagnetic power in the laboratory frame is

$$\eta = P_f/P_b \tag{B5}$$

where $P_b = \sigma_0 Lc\beta_{0\parallel}(\gamma_0 - 1)m_0c^2$ is the beam power, σ_0 is the particle surface density, and $\gamma_0 = (1 - \beta_{0\parallel}{}^2 - \beta_{0\perp}{}^2)^{-1/2}$. Combining (B4) and (B5) and using the relationship $a(B_0\mu')^2\omega_0'/(4\pi m_0c^2\Omega_0') = \sigma_0'$, we obtain

$$\eta = \frac{\sigma_0'}{\sigma_0}\gamma_{0\parallel}{}^2\frac{(\gamma_{0\perp}' - 1)}{(\gamma_0 - 1)}\eta'. \tag{B6}$$

Applying the relativistic transformations $\sigma_0 = \sigma_0'\gamma_0/\gamma_{0\perp}'$ and $\gamma_{0\parallel} = \gamma_0/\gamma_{0\perp}'$ to (B6), the power efficiency takes the simple form

$$\eta = \frac{\gamma_0(\gamma_{0\perp}' - 1)}{\gamma_{0\perp}'(\gamma_0 - 1)}\eta'. \tag{B7}$$

For a more direct derivation of (B7), we consider the relativistic Lorentz transformation of total field energy in the beam frame to the laboratory frame. Since the field momentum in the beam frame is zero, we have

$$W_f = \gamma_{0\parallel}W_f' = \gamma_{0\parallel}\eta' W_b' \tag{B8}$$

where W_f and W_b are the total field and particle energy in the laboratory frame. The power in the electromagnetic field can be written as

$$P_f = v_{0\parallel}W_f/\Delta z = v_{0\parallel}\eta' W_b'/\Delta z \tag{B9}$$

where Δz is the axial extent of the volume element which contains the total field energy W_f. The total beam energy W_b' in the beam frame can be written as

$$W_b' = \eta_b'(\gamma_{0\perp}' - 1)m_0c^2A\Delta z' \tag{B10}$$

where $A = 2r_LL$ is the cross-sectional area of the beam and $\Delta z'$ is the axial extent of the volume element in the beam frame. Substituting (B10) into (B9) and using the relationships $\eta_b'\Delta z' = \eta_b\Delta z$ and $\gamma_{0\parallel} = \gamma_0/\gamma_{0\perp}'$ yields the result

$$P_f = \frac{\gamma_0(\gamma_{0\perp}' - 1)}{\gamma_{0\perp}'(\gamma_0 - 1)}\eta' P_b$$

which defines the efficiency transformation in (B7).

Acknowledgment

The authors wish to thank W. M. Manheimer, V. L. Granatstein, and E. Ott for their useful comments and suggestions.

References

[1] R. Q. Twiss, "Radiation transfer and the possibility of negative absorption in radio astronomy," *Australian J. Phys.*, vol. 11, pp. 564–579, 1958.
[2] J. Schneider, "Stimulated emission of radiation by relativistic electrons in a magnetic field," *Phys. Rev. Lett.*, vol. 2, pp. 504–505, 1959.
[3] A. V. Gaponov, "Interaction between electron fluxes and electromagnetic waves in waveguides," *Izv. VUZ., Radiofizika*, vol. 2, pp. 450–462, 1959, and "Addendum," *Izv. VUZ., Radiofizika*, vol. 2, p. 836, 1959.
[4] R. H. Pantell, "Backward-wave oscillations in an unloaded guide," *Proc. IRE*, vol. 47, p. 1146, 1959.
[5] J. L. Hirshfield and J. M. Wachtel, "Electron cyclotron maser," *Phys. Rev. Lett.*, vol. 12, pp. 533–536, 1964.
[6] J. L. Hirshfield, I. B. Bernstein, and J. M. Wachtel, "Cyclotron resonance interaction of microwaves with energetic electrons," *J. Quantum Electronics*, vol. QE-1, pp. 237–245, 1965.
[7] J. B. Bott, "A powerful source of millimeter wavelength electromagnetic radiation," *Phys. Letters*, vol. 14, pp. 293–294, 1965. (Bott does not explicitly state the mechanism involved in his experiment.)
[8] R. L. Schriever and C. C. Johnson, "A rotating beam waveguide oscillator," *Proc. IEEE*, vol. 54, pp. 2029–2030, 1966. (In this reference efficiencies of ~10 percent were reported. The mechanism was not specified as the cyclotron maser instability.)
[9] J. M. Wachtel and J. L. Hirshfield, "Interference beats in pulse-stimulated cyclotron radiation," *Phys. Rev. Lett.*, vol. 17, pp. 348–351, 1966.
[10] M. Friedman, D. A. Hammer, W. M. Manheimer, and P. Sprangle, "Enhanced microwave emission due to the transverse energy of a relativistic electron beam," *Phys. Rev. Lett.*, vol. 31, pp. 752–755, 1973.
[11] V. L. Granatstein, M. Herndon, P. Sprangle, Y. Carmel, and J. A. Nation, "Gigawatt microwave emission from an intense relativistic electron beam," *Plasma Physics*, vol. 17, pp. 23–28, 1975.
[12] V. L. Granatstein, P. Sprangle, M. Herndon, R. K. Parker, and S. P. Schlesinger, "Microwave amplification with an intense relativistic electron beam," *J. Appl. Phys.*, vol. 46, pp. 3800–3805, 1975.
[13] V. L. Granatstein, P. Sprangle, R. K. Parker, and M. Herndon, "An electron synchrotron maser based on an intense relativistic electron beam," *J. Appl. Phys.*, vol. 46, pp. 2021–2028, 1975.
[14] N. I. Zaytsev, T. B. Pankratova, M. I. Petelin, and V. A. Flyagin, "Millimeter and submillimeter waveband gyrotrons," *Radiotekhnika i Electronica*, vol. 19, pp. 1056–1060, 1974.
[15] D. V. Kisel', G. S. Korablev, V. G. Navel'yev, M. I. Petelin, and Sh. E. Tsimring, "An experimental study of a gyrotron, operating at the second harmonic of the cyclotron frequency, with optimized distribution of the high frequency field," *Radio Engineering and Electronic Physics*, vol. 19, pp. 95–100, 1974.
[16] H. Jory, "Investigation of electronic interaction with optical resonators for microwave generation and amplification," Research and Development Technical Report, ECOM-01873-F (1968), Varian Associates.
[17] V. L. Bratman and A. E. Tokarev, "On the theory of the relativistic cyclotron-resonance maser," *Radiofizika*, vol. 17, pp. 1224–1228, 1974.
[18] V. V. Zhelznyskov, *Izv. VUZ., Radiofizika*, vol. 3, pp. 1–57, 1960.
[19] E. Ott and W. M. Manheimer, "Theory of microwave emission by velocity-space instabilities of an intense relativistic electron beam," *IEEE Trans. Plasma SC.*, vol. PS-3, pp. 1–5, 1975.
[20] A. V. Gaponov, M. I. Petelin, and V. K. Yulpatov, "The induced radiation of excited classical oscillators and its use in high frequency electronics," *Izv. VUZ., Radiofizika*, vol. 10, pp. 1414–1453, 1967.
[21] V. A. Zhurakovskiy, "Using an averaging method to integrate nonlinear equations for phase-synchronous instruments," *Radiotekhnika i Electronika*, vol. 9, p. 1527, 1964.
[22] G. N. Rapoport, A. K. Nemak, and V. A. Zhurakovskiy, "Interaction between helical electron beams and strong electromagnetic cavity fields at cyclotron frequency harmonics," *Radiotekhnika i Electronika*, vol. 12, p. 587, 1967.
[23] G. S. Nusinovich and R. E. Erm, *Elektronnaya Tekhnika*, Sec. 1, Elektronika SVCH, no. 2, p. 55, 1972.
[24] E. M. Demidovich, I. L. Kovalev, A. A. Kurayev, and F. C. Shevchenko, "Efficiency optimized cascaded circuits utilizing the cyclotron resonance," *Radiotekhnika i Electronika*, vol. 18, p. 2097, 1973.
[25] P. Sprangle and W. M. Manheimer, "Coherent nonlinear theory of a cyclotron instability," *Phys. Fluids*, vol. 18, pp. 224–230, 1975.
[26] In [18], a dispersion relation is derived, which is a special case of (1). In this reference, the transverse wave number is assumed to vanish, $ck_\perp = 0$. It is found that instability can still exist for finite k_0 if $\beta_{0\perp}{}^2 > 1 - \beta_{0\parallel}$. The growth rate is given by $\Gamma = \omega_b/\sqrt{2}(1 - \beta_{0\parallel} - \beta_{0\perp}{}^2)^{1/2}$ for $l = 1$ and $n \doteq 0$.
[27] It should be noted that the right-hand side of the expression for $\beta_{\perp,\mathrm{crit}}$ is also a function of $\beta_{\perp,\mathrm{crit}}$. In the given expression for $\beta_{\perp,\mathrm{crit}}$, $\beta_\perp$ should be replaced by $\beta_{\perp,\mathrm{crit}}$.
[28] "Status and objectives of Tokomak systems for fusion research," pp. 53–55, USAEC, Wash. 1295.
[29] V. V. Aliekaev and Yu. I. Arsenyev, "High frequency power sources applied for plasma heating in TM-3 Tokamak," *Proc. Conf. on Plasma Heating*, Grenoble, France, 1976.
[30] W. M. Stacey, Jr., C. C. Baker, and M. Roberts, "Tokomak experimental power reactor," *Proc. VI Int. Conf. Plasma Physics and CTR-IAEA*, pp. 215–216, Berchtesgarden, F.R.G., Oct. 1976.